A fiber-based microcavity for strong coupling of excitons

Julian David Spanier

Masterarbeit in Physik
angefertigt im Physikalischen Institut
vorgelegt der
Mathematisch-Naturwissenschaftlichen Fakultät
der
Rheinischen Friedrich-Wilhelms-Universität
Bonn

April 2026

I hereby declare that this thesis was formulated by myself and that no sources or tools other than those cited were used.

Bonn, 13.04.2026
Bonn, Date

Signature

Gutachter und Betreuer: Prof. Dr. Michael Köhl

Gutachter: Prof. Dr. Stefan Linden

Contents

CHAPTER 1

Introduction

The study of light-matter interactions is a central topic of modern quantum optics and condensed matter physics research. When a semiconducting material is excited by a photon, an electron is lifted from the valence band into the conduction band. This electron is bound to a corresponding hole in the valence band via Coulomb attraction, forming a quasi-particle known as an exciton [1]. Under the right conditions, when a quantum emitter such as an exciton strongly interacts with a confined electromagnetic field, the system can enter the strong coupling regime. In this regime, the coherent exchange between photonic and excitonic states happens on a timescale faster than their respective decay processes, leading to the formation of hybrid light-matter states known as exciton-polaritons. Exciton-polaritons are bosonic in nature and have a very low effective mass of about 10^{-4} of the free electron mass. Consequently, they feature a large de Broglie wavelength, enabling Bose-Einstein-condensation at temperatures of a few Kelvin rather than the $10^{-6}K$ or lower that are necessary in conventional atomic gases [2].

Creating these polariton states requires a material with robust excitonic resonances and a high exciton binding energy. Transition metal dichalcogenides (TMDs), such as $MoSe_2$ and WSe_2, fulfill this requirement, making them popular candidates for experiments in solid-state quantum optics [3,4]. As van der Waals materials, the layers of TMD crystals are bound to each other by relatively weak forces, allowing for the mechanical exfoliation of individual layers down to a single monolayer using simple mechanical methods [5]. As opposed to bulk TMDs, these isolated monolayers exhibit a direct bandgap, which enables efficient optical excitation of the material [6]. Furthermore, the reduced dielectric screening in two-dimensional materials leads to high exciton binding energies, which is favorable for the observation of strong coupling [7]. Strong coupling in two-dimensional atomic crystals was first experimentally observed in 2014 by Liu et al. using a MoS_2 monolayer

embedded in a monolithic dielectric microcavity [8]. Because their approach lacks the possibility of tuning the cavity length, they relied on angle-resolved measurements to observe the hybridization into polaritons and polariton dispersion. In 2015, Dufferwiel et al. integrated van der Waals heterostructures into an open, tunable microcavity [9]. This setup allowed them to demonstrate the formation of exciton-polaritons in a $MoSe_2$ monolayer by directly scanning the cavity length, bypassing the need for angle-resolved measurement techniques. These experiments prove the viability of TMDs for creating robust polaritonic systems. However, reaching the strong coupling regime imposes strict requirements on the optical microcavity, such as a minimal cavity length and extremely low optical losses.

Fiber-based Fabry-Pérot microcavities (FFPCs) are well suited for fulfilling these requirements, as they allow for very small physical mirror separations due to their small diameter. To achieve the highly curved mirror surfaces, Hunger et al. developed a method utilizing a CO_2 laser to machine smooth, Gaussian-shaped depressions onto the fiber end-faces [10].

In this thesis, we design, fabricate, and characterize a tunable, fiber-based microcavity specifically designed to reach the strong coupling regime with TMD excitons at cryogenic temperatures. Following the successful processing and high-reflectivity DBR coating of 144 individual fiber mirrors, we integrate the components into both an ambient-temperature testing platform and a custom-built cryogenic cavity assembly. We analyze the spatial alignment, mode coupling efficiency, and overall geometric limits of the final resonator configuration. Finally, we demonstrate high cavity finesse values around 3000 and integrate a 2D material sample into the cavity, showcasing the system's potential for future strong coupling experiments.

CHAPTER 2

Theoretical Considerations

The study of light-matter interactions is a central topic of modern quantum optics and condensed matter physics research. These interactions can be enhanced by using optical resonators to confine the electromagnetic field, leading to phenomena such as strong coupling and the formation of hybrid light-matter states known as polaritons. This chapter provides the theoretical foundation for understanding strong coupling between excitons and photons in two-dimensional transition metal dichalcogenides embedded in optical microcavities.

2.1 Excitons in transition metal dichalcogenides

Van der Waals (vdW) materials include a variety of layered crystals that exhibit a wide range of properties, including metallic, dielectric, and semiconducting behavior. Within a single layer of these crystals, atoms are bound by strong covalent interactions, however the individual layers are held together by comparatively weak van der Waals forces. This stark difference in bonding strength allows these materials to be isolated into single atomic layers using relatively simple mechanical exfoliation techniques, for example using adhesive tape [5,6]. Monolayer or multilayer flakes of different vdW materials can be stacked to form custom heterostructures with specifically engineered physical properties. Transition metal dichalcogenides (TMDs) are a prominent category of these vdW materials. Due to their exceptionally strong excitonic resonances, TMDs have become established subjects of research in solid-state quantum optics. Their crystal structure contains a transition metal atom which forms a covalent bond with two chalcogen atoms, for example $MoSe_2$ or WSe_2. While bulk TMDs are indirect band gap semiconductors, reducing them to a single monolayer creates a direct band gap at the K and K' points of the hexagonal

Brillouin zone [6,11]. This direct gap allows for the efficient absorption and emission of light, making TMD monolayers an ideal candidate for studying light-matter interactions. The phenomenon at the focus of this thesis is the exciton, a quasi-particle consisting of a Coulomb-bound electron-hole pair. The physical properties of excitons in monolayer TMDs differ drastically from those in bulk semiconductors: In monolayer TMDs, the electric field that binds the electron and hole together extends into the surrounding material or vacuum instead of a bulk crystal with large dielectric constant, resulting in a reduced screening effect of the Coulomb attraction. This reduced screening leads to exciton binding energies on the order of several hundred meV. As a result, the Bohr radius a_{B} is reduced in monolayers compared to bulk material, leading to a large oscillator strength due to its $1/a_{\mathrm{B}}^2$ dependence [3,7].

2.2 Strong coupling of excitons in optical cavities

The goal for integrating monolayer TMD materials into an optical microcavity is to create an environment where the light-matter interaction is greatly enhanced. Under the right conditions, the system can enter the strong coupling regime, where the eigenstates of the system transform into hybrid light-matter states called exciton-polaritons. We will see that two properties of the cavity fundamentally influence the ability to enter the strong coupling regime: A short cavity length is necessary to achieve a high coupling strength between photons and excitons, while the decay rate of cavity photons and excitons must be kept small.

A Jaynes-Cummings Hamiltonian can be used to describe the interaction as a two-level system [12]:

$$\hat{H} = \sum_{\boldsymbol{k}} E_x(k)\hat{x}_{\boldsymbol{k}}^{\dagger}\hat{x}_{\boldsymbol{k}} + \sum_{\boldsymbol{k}} E_{\mathrm{cav}}(k)\hat{c}_{\boldsymbol{k}}^{\dagger}\hat{c}_{\boldsymbol{k}} + \sum_{\boldsymbol{k}} \hbar\Omega_{\mathrm{R}}\left(\hat{x}_{\boldsymbol{k}}^{\dagger}\hat{c}_{\boldsymbol{k}} + \hat{c}_{\boldsymbol{k}}^{\dagger}\hat{x}_{\boldsymbol{k}}\right) \tag{2.1}$$

Where $x_{\boldsymbol{k}}^{\dagger}$ and $c_{\boldsymbol{k}}^{\dagger}$ are the creation operators for an exciton and a cavity photon with wavevector $\boldsymbol{k}$, respectively. The Rabi frequency Ω_{R} is given by [12,13]:

$$\Omega_{\mathrm{R}} = \left[\frac{4\pi\omega_{\mathrm{cav}}}{L} f_{\mathrm{X}}\right]^{\frac{1}{2}} \frac{E(z)}{E_{\mathrm{max}}} \tag{2.2}$$

With the cavity field frequency ω_{cav}, cavity length L and oscillator strength f_{X}. Diagonalizing the Hamiltonian results in two new eigenstates called upper polariton (UP) and lower polariton (LP), separated by the vacuum Rabi splitting $\hbar\Omega_R$ [1,12]. The energy of the two polariton branches is given by:

$$E_{\pm} = \frac{1}{2}(E_{\text{cav}} + E_x) \pm \frac{1}{2}\sqrt{\Delta^2 + 4\hbar^2\Omega_R^2} \tag{2.3}$$

where $\Delta = E_{\text{cav}} - E_x$ is the detuning of the cavity resonance from the exciton resonance.

The transition from separate photon and exciton states to a coupled light-matter system is determined by the coherent exchange rate $g \approx \Omega_R/2$ [12] and the incoherent decay rates of the cavity photons κ and the excitons γ, which need to fulfill the strong coupling condition:

$$g > \kappa, \gamma \tag{2.4}$$

In an optical cavity, the lifetime of photons is determined by the intra-cavity losses, and is related to the cavity finesse $\mathcal{F}$ and the cavity length L by:

$$\kappa = \frac{\pi c}{2L\mathcal{F}} \tag{2.5}$$

The homogeneous linewidth γ of the of the exciton resonance is composed of a temperature-independent radiative part γ_0 and a temperature-dependent non-radiative part $\gamma_{\text{non-rad}}(T)$ caused by phonon scattering [11]. At cryogenic temperatures, $\gamma_{\text{non-rad}}(T)$ is minimized, making it easier for the system to satisfy the strong coupling condition. In order to maximize the coupling strength g and to be able to reach the strong coupling regime, we need to minimize the cavity length, while at the same time keeping $\kappa < g$.

The hybridization into polaritonic states introduces some interesting new properties for the coupled system: The optical cavity modifies the spontaneous emission of the TMD monolayer, which can inhibit the radiative decay and effectively reduce the natural linewidth of the exciton. Furthermore, the effective mass of a polariton is extremely small due to the hybridization with the photonic component [14]. For an in-plane momentum $k_{\parallel} \approx 0$, this effective mass is approximately four orders of magnitude lighter than that of a bare exciton, enabling Bose-Einstein-condensation at temperatures of a few Kelvin rather than the $10^{-6}K$ or lower that are necessary in conventional atomic gases [2].

2.3 Resonator optics at the micrometer scale

Understanding the behavior and distribution of the electromagnetic field inside the micro-cavity is essential for creating a cavity design suitable for observing strong coupling of excitons to cavity photons. Optical cavities can be constructed using a variety of mirror geometries, such as planar, plano-concave, or confocal configurations. A cavity geometry is considered optically stable if a beam remains spatially confined within the resonator

without diverging. Planar cavities are inherently unstable, as any small misalignment of the mirrors causes the beam to diverge and eventually escape the cavity, which is why spherical mirrors are commonly used to create stable resonators. For our experiments, we implement a plano-concave cavity configuration consisting of one flat mirror and one concave curved mirror. This configuration is stable for cavity lengths L smaller than the radius of curvature R of the curved mirror. Another reason for using this configuration is that the flat mirror provides a necessary planar substrate to deposit a 2D material sample.

The spatial distribution of the electromagnetic field amplitude inside an optical resonator with spherical mirrors is described by the Hermite-Gaussian modes. Along the optical axis (z-axis), the radius w of a mode is given by

$$w(z) = w_0 \sqrt{1 + \left(\frac{\lambda}{\pi} \frac{z}{w_0^2}\right)^2} \tag{2.6}$$

where w_0 is the waist radius (radius at the thinnest part of the mode) and λ is the wavelength of the used light. The origin of the z axis is defined as the position of the mode waist. [15] The mode profile is entirely defined by the wavelength λ and its waist radius w_0, which in turn is defined by the radii of curvature (ROC) R_1 and R_2 of the mirrors and the cavity length L:

$$w_0 = \sqrt{\frac{\lambda}{\pi}} \left(\frac{(R_1 - L)(R_2 - L)(R_1 + R_2 - L)}{(R_1 + R_2 - 2L)^2} \right)^{1/4} \tag{2.7}$$

In the case of plano-concave resonators, such as those this thesis focuses on, one of the ROCs approaches infinity, simplifying Equation (2.7):

$$\lim_{R_2 \to \infty} w_0 = \sqrt{\frac{\lambda}{\pi}} (L(R_1 - L))^{1/4} \tag{2.8}$$

An example of the mode profile in a plano-concave cavity is shown in Figure 2.1. The monolayer TMD samples we target typically have a diameter of about 5 µm to 10 µm, setting a limit for the mode diameter on the sample. Reaching even smaller mode diameters is desirable to avoid sampling over possible inhomogeneities on the sample, which could negatively affect the coupling strength. For possible future experiments with confined excitons, the coupling strength g heavily depends on the spatial overlap between the cavity field and the exciton wave function. Because a confined exciton typically extends over only about 10 nm, this would put an even stronger constraint on the mode diameter.

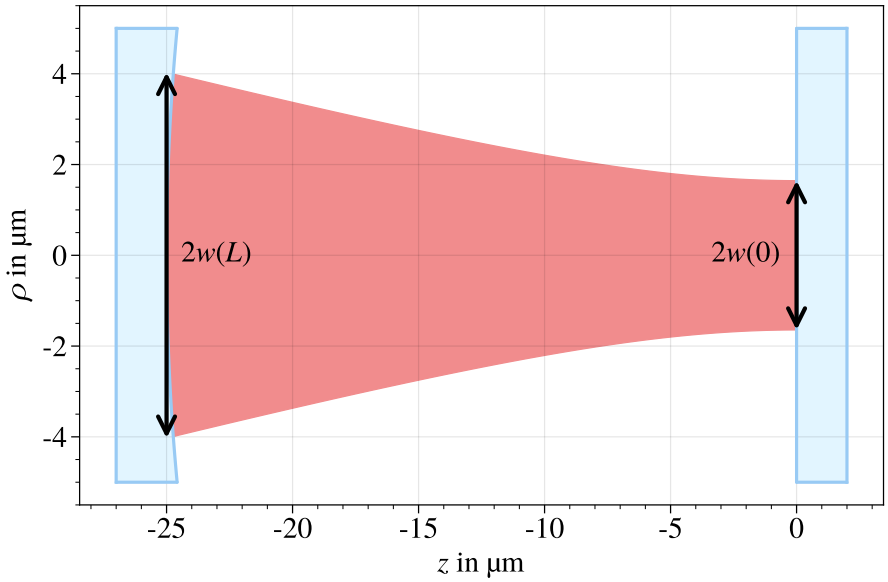

Figure 2.1: Schematic representation of the Gaussian mode profile in a plano-concave microcavity. The position of the minimum mode waist $w(0)$ is defined by the planar mirror at $z = 0$. The coordinate ρ specifies the radial distance from the optical axis.

Light of a certain frequency is resonant in an optical resonator if the light wave is exactly replicated after a round trip, which consists of reflections at both mirrors and propagation over the length L in each direction for a total propagation length of $2L$. At cavity lengths in the regime of a few wavelengths, the resonance condition is no longer dominated by the phase accumulated during light propagation in the cavity: Additionally, one has to consider the effects of the Gouy phase shift and dispersive properties of the mirrors in order to accurately model the resonator. For the distributed bragg reflector (DBR) mirrors we use, the phase shift upon reflection φ_{DBR} varies for different wavelengths, as illustrated in Figure 2.2. In order to fulfill the resonance condition, the accumulated round trip phase φ_{RT} has to become a multiple of 2π:

$$\begin{aligned} \varphi_{\mathrm{RT}}(\omega) &= \frac{2\omega L}{c} + \varphi_{\mathrm{DBR}}(\omega) - 2(p+q+1)\Delta\zeta \\ &= \frac{2\omega L}{c} + \Delta\varphi(\omega) \stackrel{!}{=} m \cdot 2\pi \end{aligned} \tag{2.9}$$

where n is the longitudinal mode order, p and q are the transversal mode orders, φ_{DBR} is the added phase shift upon reflection from both mirrors and $\Delta\zeta = \arcsin\left(\sqrt{L/R}\right)$ is the Gouy phase shift. From this follows an expression for the resonance frequencies ω_{mpq}:

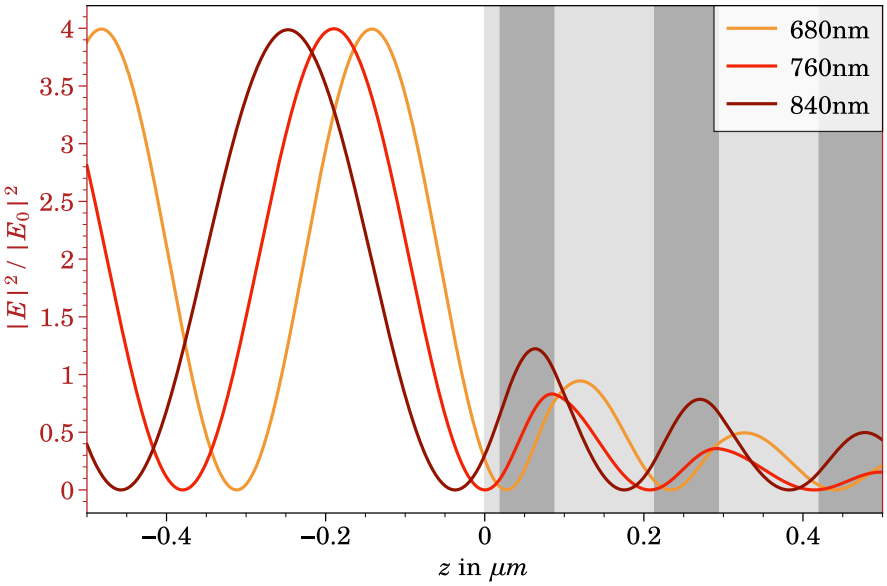

Figure 2.2: An example transfer matrix simulation of waves with different wavelengths reflecting from the same DBR mirror. The phase shift upon reflection causes the antinode of the electric field to be shifted away from the surface of the mirror for wavelengths deviating from 760 nm. A plot showing the phase shift for a continuous wavelength range is shown in Figure A.1.

$$\omega_{mpq} = \frac{\pi c}{L}\left(m - \frac{1}{2\pi}(\varphi_{\mathrm{DBR}}(\omega) + 2(p+q+1)\Delta\zeta)\right) \tag{2.10}$$

As m decreases, the resonance frequencies become less uniformly spaced, meaning that the usual definition of a constant free spectral range (FSR) is no longer strictly applicable.

Furthermore, the Gouy phase $\Delta\zeta$ is modified by the modal penetration depth L_D. This length describes the distance light travels within the DBR layers and is defined by the group delay upon reflection τ_{gd}, modified by a scaling factor β which depends on the refractive indices of the DBR layers [16]:

$$L_D = \beta\frac{c\tau_{\mathrm{gd}}}{2} \quad \text{with} \quad \beta = \frac{n_{\mathrm{in}}^2}{2}\left(\frac{1}{n_{\mathrm{L}}^2} + \frac{1}{n_{\mathrm{H}}^2}\right) \tag{2.11}$$

where n_{L} and n_{H} are the low and high refractive indices of the DBR layers, respectively and n_{in} is the refractive index of the medium in front of the mirror. The group delay τ_{gd} is related to the phase shift upon reflection φ_{DBR} by the following expression:

$$\tau_{\mathrm{gd}} = \frac{1}{2\pi}\frac{d\varphi_{\mathrm{DBR}}}{d\nu} \tag{2.12}$$

The group delay curve for our two DBR coatings is shown in Figure A.2. For two different DBR mirrors with modal penetration depths L_{D1} and L_{D2}, the corrected Gouy phase is then given by:

$$\Delta\zeta = \arcsin\left(\sqrt{\frac{L + L_{D1} + L_{D2}}{R}}\right) \tag{2.13}$$

Accounting for these specific penetration depths is important for accurately analyzing cavity spectra, which is applied when evaluating the cavity finesse in Section 4.3. Because L_D influences the imaging properties of the DBR, the effective cavity length that determines the stability and the mode waist radius w_0 is increased. For a hemispherical resonator, the corrected waist radius is given by:

$$w_0 = \sqrt{\frac{\lambda}{\pi}}[(L + L_{D1} + L_{D2})(R_1 - (L + L_{D1} + L_{D2}))]^{1/4} \tag{2.14}$$

for our two different coatings, the modal penetration depths are 82.1 nm (B-12752-02) and 83.9 nm (B-12752-03) at $\lambda = 750$ nm, which is the center wavelength of the stopband for both coatings.

2.4 Cavity finesse

A common way to characterize the performance of an optical resonator is its finesse $\mathcal{F}$. The finesse is defined as the ratio of the free spectral range ν_{FSR} to the full width at half maximum (FWHM) linewidth $\delta\nu$ of the cavity transmission peaks:

$$\mathcal{F} = \frac{\nu_{\mathrm{FSR}}}{\delta\nu} = \frac{c}{2L\delta\nu} \tag{2.15}$$

The free spectral range defines the frequency separation between adjacent longitudinal modes and scales inversely with the effective cavity length. Reducing the cavity length shortens the photon round-trip time, thus increasing the number of reflections the per unit time. Since a fraction of energy is lost from the cavity on every reflection, this higher reflection rate decreases the lifetime of photons in the cavity. Thus, for a resonator with a given finesse, shortening the cavity inherently broadens the resonance linewidth. The finesse itself is determined by the total optical losses of the circulating cavity field during

a single round trip. These losses consist of the mirror transmittivities T_1 and T_2, along with any internal scattering or absorption $\mathcal{L}_{\text{cav}}$. For low total losses, the finesse can be approximated by [15]:

$$\mathcal{F} \approx \frac{2\pi}{T_1 + T_2 + \mathcal{L}_{\text{cav}}} \tag{2.16}$$

Consequently, any scattering or absorption losses on the order of the mirror transmittivities can significantly reduce the finesse and broaden the cavity resonance.

CHAPTER 3

Fiber-based Fabry-Pérot microcavity

To reach the strong coupling regime, our optical cavity must simultaneously exhibit a narrow cavity linewidth and an exceptionally short cavity length, as explained in Section 2.2. Fiber-based cavities are well suited for this purpose, as the small diameter of the fiber surface allows for the implementation of short cavity lengths in the micrometer range. Our experiment uses a fiber-based Fabry-Pérot microcavity (FFPC) consisting of a planar fused silica substrate and a laser-machined optical fiber, acting as the curved mirror. We create the curved mirror profile by applying a single focused pulse from a CO_2 laser to the cleaved end-face of the fiber. The localized thermal absorption causes rapid melting and evaporation of the glass, naturally forming a smooth, Gaussian-shaped depression [10]. At the center of this depression, the resulting geometric profile closely approximates a spherical mirror. To achieve the high finesse required for our experiments, both the machined fiber and the planar substrate are subsequently coated with custom distributed Bragg reflectors (DBR).

3.1 Fiber machining setup

A critical component of our fiber-cavities is the concave profile of the fiber end-face ("dimple"), which defines the mode geometry of the cavity, see Section 2.3. To shape the surface of the fiber mirrors, we use a specialized CO_2 laser setup located in the *Fiberlab*, a shared laboratory specialized on working with and modifying optical fibers at the University of Bonn. A schematic representation of the setup is shown in Figure 3.1. The setup currently uses a *Coherent Diamond C-30+* continuous wave CO_2 laser with an output power of up to 30 W and a wavelength of about 9.3 µm. The CO_2 laser beam is initially collimated by a telescopic lens arrangement. To precisely control the laser pulses delivered

to the fiber end-face, the beam passes through an acousto-optic modulator (AOM). This AOM allows us to control both the optical power and the duration of the pulse used for machining the fiber. Prior to machining, we can check the incident optical power shortly before the fiber by utilizing a flip-mirror, which deflects the beam onto a powermeter. The setup also incorporates an interferometric microscope parallel to the beam path, equipped with a Mirau objective, which is used for precise positioning of the fiber as well as surface analysis before and after processing. A 3D translation stage is used to precisely move the fiber between the microscope and the laser beam. After calibrating this spatial offset, we can precisely center the fiber in the laser beam by first centering it in the microscope and then moving it by the predetermined offset.

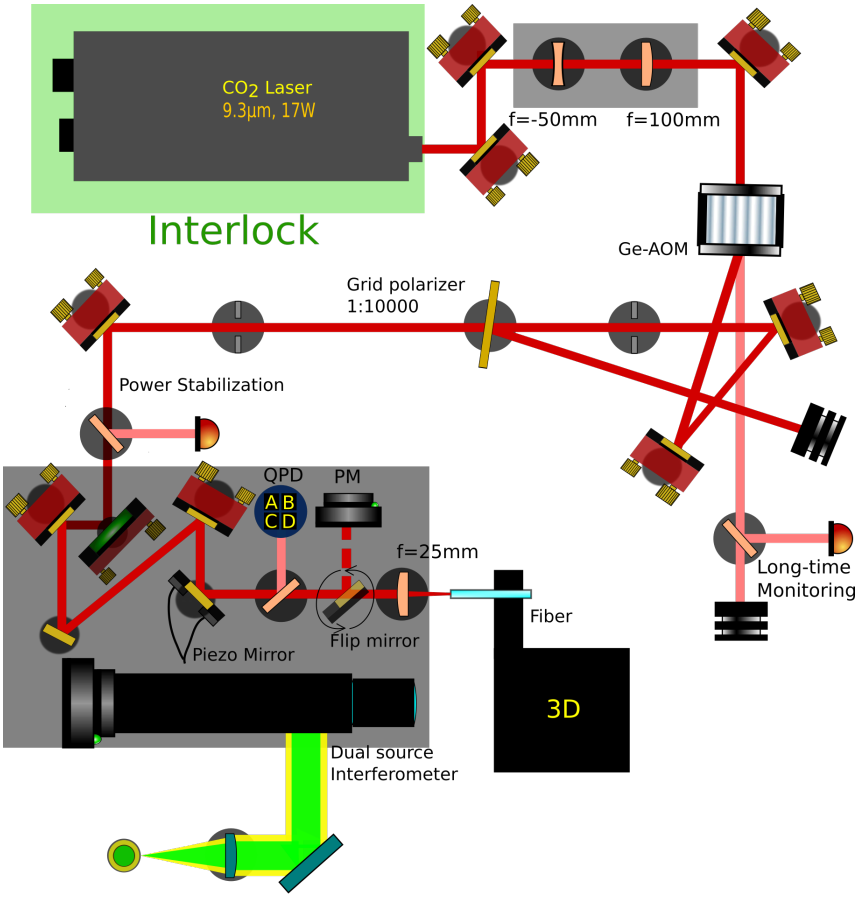

Figure 3.1: Schematic of the CO_2 laser setup at the *Fiberlab*. A 3D translation stage in combination with an interferometric microscope allows for precise positioning of the fiber.
Image taken from: [17]

3.2 Design and limits of the cavity geometry

The ablation from the CO_2 laser results in a concave dimple with an approximately Gaussian profile that can be geometrically described using three quantities: the depth t, the radius of curvature R at the center, and the useful diameter D, as shown in Figure 3.2. At the center of this depression, the dimple profile closely approximates a spherical mirror with a local radius of curvature R. Following the model presented by Hunger et al. [10], the useful diameter D of a fiber mirror is given by the full width at $1/e$ of the Gaussian dimple profile and can be approximated by:

$$D^2 \approx 8tR \tag{3.1}$$

The useful diameter indicates the diameter around the center of the Gaussian dimple profile, in which it can be approximated by a spherical shape. In the following analysis, we also use D as a figure of merit for comparing the different fiber profiles.

We can define the resonator's mode size by adjusting the properties of the dimple on the fiber end-face. To minimize the sampling of inhomogeneities across the TMD monolayer, it is necessary to achieve a small beam waist w_0 of about $(1-2)\,\mu\text{m}$. As discussed in Section 2.3, achieving modes of this size requires a mirror with a correspondingly small radius of curvature (ROC). However, decreasing the ROC requires creating a deeper dimple, which presents a geometric tradeoff between minimum mode waist radius and minimum cavity length. The minimum physical mirror separation is geometrically defined by the dimple depth t. However, the effective minimum cavity length L_{min} is not exclusively defined by this, as the electromagnetic field extends into the DBR layers, as discussed in Section 2.3. This penetration depth increases the effective optical path length

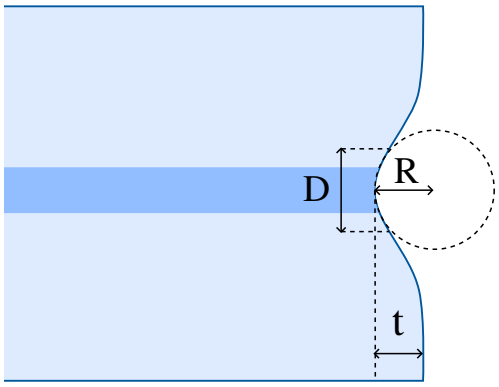

Figure 3.2: Sketch of the dimple geometry on a fiber end-face with the characteristic parameters depth t, radius of curvature R and useful diameter D. The proportions of the dimple are not to scale and exaggerated for better visibility.

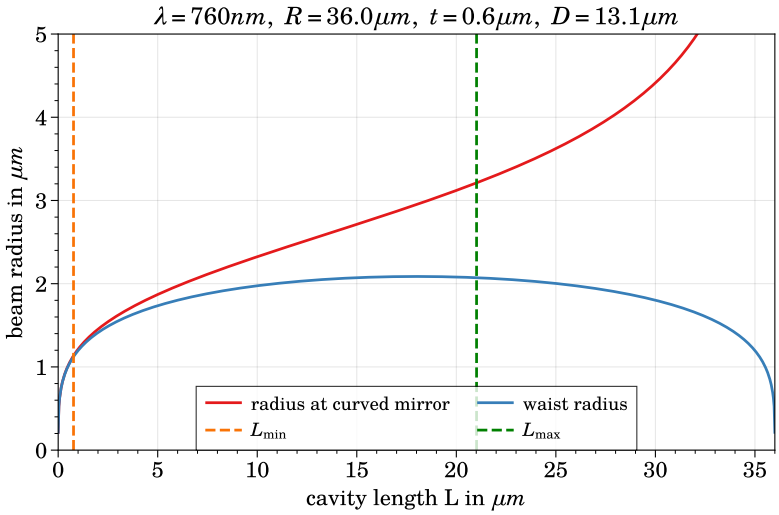

Figure 3.3: Example of beam radii in a plano-concave cavity at the curved mirror and at the planar mirror (coinciding with the beam waist) at different positions along the cavity axis. L_{min} is the minimum cavity length, limited by the dimple depth and the penetration depth into the DBR layers, while L_{max} is the maximum cavity length, limited by clipping losses at the curved fiber mirror.

of the cavity and has to be taken into account when calculating the mode geometry. In the case of our mirror coatings, we calculate the modal penetration depths for our two different coatings using transfer matrix calculations based on the thicknesses of the coating layers. They are 82.1 nm (coating B-12752-02) and 83.9 nm (coating B-12752-03) at $\lambda =$ 750 nm, which is the center wavelength of the stop-band for both coatings.

On the other hand, the maximum usable cavity length L_{max} is limited by clipping losses at the curved fiber mirror. While the center of the Gaussian dimple profile closely approximates a spherical mirror, it deviates more significantly at larger radii. As the mirror separation L increases, the radius of the cavity mode at the position of the curved fiber mirror expands, as shown in Figure 3.3. As the mode begins to sample the regions of the dimple where the deviation becomes significant compared to the wavelength, a part of the reflected phase front is scattered out of the cavity mode, lowering the finesse. The clipping loss per reflection on a mirror with effective diameter D is then given by [10]:

$$\mathcal{L}_{\text{cl}} = e^{-2(D/2)^2/w_m^2} \tag{3.2}$$

where w_m is the mode radius on the fiber-mirror. For the design of our cavities, we adapt the definition of L_{max} from Hunger et al. [10] as the threshold cavity length at which these clipping losses cause a 10% reduction in the total cavity finesse, corresponding to

$\mathcal{L}_{\text{cl}} < 2\pi/(10\mathcal{F})$. This restriction limits the mode radius on the mirror to $w_m \leq w_{\text{cl}} := \alpha_{\text{cl}}(D/2)$. The scaling factor α_{cl} is given by [10]:

$$\alpha_{\text{cl}} = \sqrt{\frac{2}{-\ln(2\pi/(10\mathcal{F}))}} \tag{3.3}$$

which is strictly dependent on the overall finesse. The maximum cavity length L_{max} can then be determined by rearranging Equation (2.8):

$$L_{\text{max}} = \frac{2\pi}{\lambda} w_0 \sqrt{w_{\text{cl}}^2 - w_0^2} \tag{3.4}$$

3.3 Fiber mirror fabrication

For the fabrication of the fiber mirrors, we utilize both *Cu600* and *Cu800* fibers manufactured by *IVG Fiber*. The *Cu600* fibers are designed for an operational wavelength range between 600 nm and 800 nm. Because our goal is to tune the microcavity to the excitonic resonances of $MoSe_2$ ($\lambda \approx 760$ nm) or WSe_2 ($\lambda \approx 720$ nm), the *Cu600* fibers are suitable for use in our experiments. In contrast, the *Cu800* fibers are designed for longer wavelengths ranging from 800 nm to 1000 nm. The inclusion of the *Cu800* fibers simply provides an further option to choose from, ensuring broader experimental flexibility for potential future experiments with different requirements. We processed a total of 144 fibers, with 96 being *Cu600* and 48 being *Cu800*.

Before a fiber can be processed in the laser setup, it must be carefully prepared and cleaved. We use copper coated fibers instead of e.g. polymer coated fibers because they are able to withstand the high temperatures during the DBR coating process. We cut the fibers to a length of 0.5 m in order to have sufficient length for routing the fiber through the final experimental assembly (see Section 4.2) and for in-place splicing. First, approximately 3 cm of the protective copper coating at the fiber end must be removed to ensure a clean and controlled split across the fiber when cleaved. We strip away the copper coating chemically by submerging the end of the fiber in a $FeCl_3$ solution for about 15 minutes. Beneath this coating, a thin carbon layer remains after the copper is removed. This layer acts as an interface between the copper coating and the fiber cladding made of glass. We observed that removing this residual carbon layer via plasma ashing before cleaving significantly improves the consistency and quality of the resulting cleaved surfaces. The plasma ashing process is performed in a *Diener Zepto* device at 100% power and 0.4 mbar of ambient air for 5 minutes. To fit the 0.5 m long fibers into the plasma ashing chamber, they are

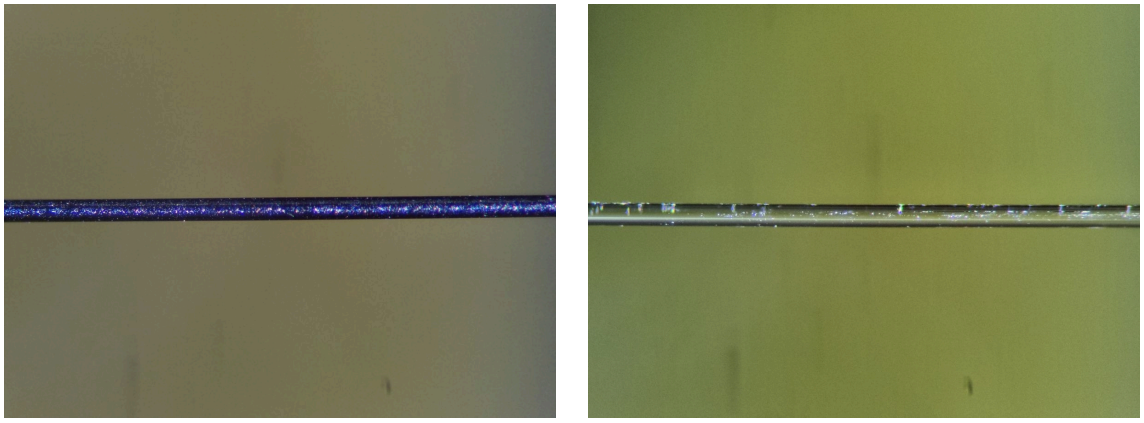

(a) before plasma ashing (b) after plasma ashing

Figure 3.4: Comparison of the fiber cladding surface before and after plasma ashing. The plasma ashing process removes the residual carbon layer, which we found to improve the consistency and quality of the subsequent cleaving process.

curled into a loop, taking care not to fall below the minimum bending radius of 10 mm. A visual comparison of the fiber before and after plasma ashing is shown in Figure 3.4.

The fiber end-face must be extremely flat and perpendicular to the optical axis. This allows us to position it close to the planar mirror, and ensures that the subsequent laser machining creates a circular dimple with minimal distortions. For the cleaving process, we use a semi-automatic cleaver (*Nyfors Autocleaver*), which allows us to precisely control the tension applied to the fiber. Additionally, the cleaver delivers largely consistent results, which is necessary for the large number of fibers that we needed to process. Achieving an

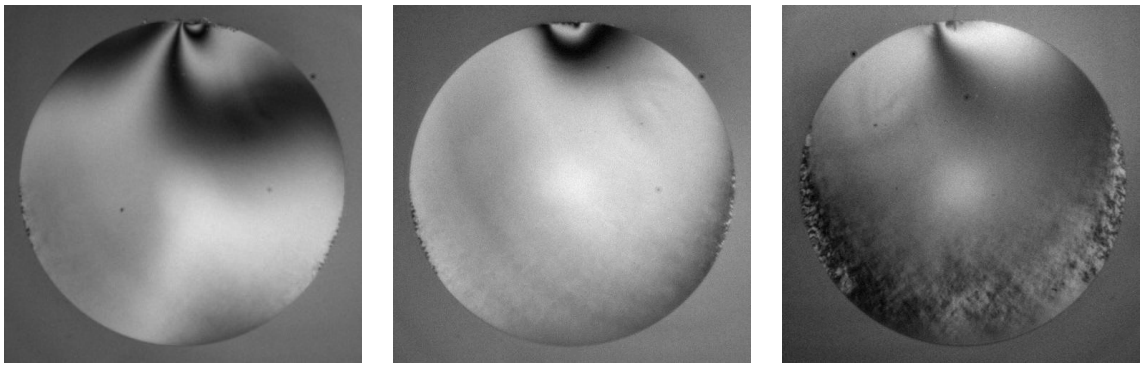

180 g 195 g 234 g

Figure 3.5: Interferometric microscope images comparing the cleave quality for different levels of applied tension. Optimal results are observed at 195 g.

optimal cleaving result relies heavily on finding the optimal tension setting. Insufficient tension frequently leads to failed cleaves or strongly curved end-faces, while excessive tension causes roughness across the surface. This behavior is illustrated in Figure 3.5. Following extensive testing, we chose a cleaving tension of 195 g for the majority of the processed fibers. Once the fiber is successfully cleaved, the resulting end-face is analyzed using the interferometric microscope. If the cleave quality is sufficient, the fiber is inserted into a custom fiber holder (see Figure 3.12), which is designed to hold up to 26 fibers, though we only filled each holder with 24 fibers, as fibers in the outer two grooves cannot always be well secured. Once a holder is filled, it can be transferred to the CO_2 laser setup to process the fibers. Aligning the position is done by centering the fiber within the microscope image, after which the translation stage moves the fiber by a predetermined offset into the beam path of the CO_2 laser. To compensate for drifts over time, this offset must be calibrated before every session. We perform this calibration by making a test dimple on a blank glass substrate and determining the deviation of the resulting dimple from the desired target position. Accordingly, we correct the stage offset between the interferometric microscope and the laser to achieve minimal offset during the actual fiber machining.

During laser machining, the end-face of the fiber is placed precisely in the laser beam's focal spot, which results in the smallest possible diameter. We find the position of the focal spot by varying the stage offset along the optical axis of the laser and analyzing

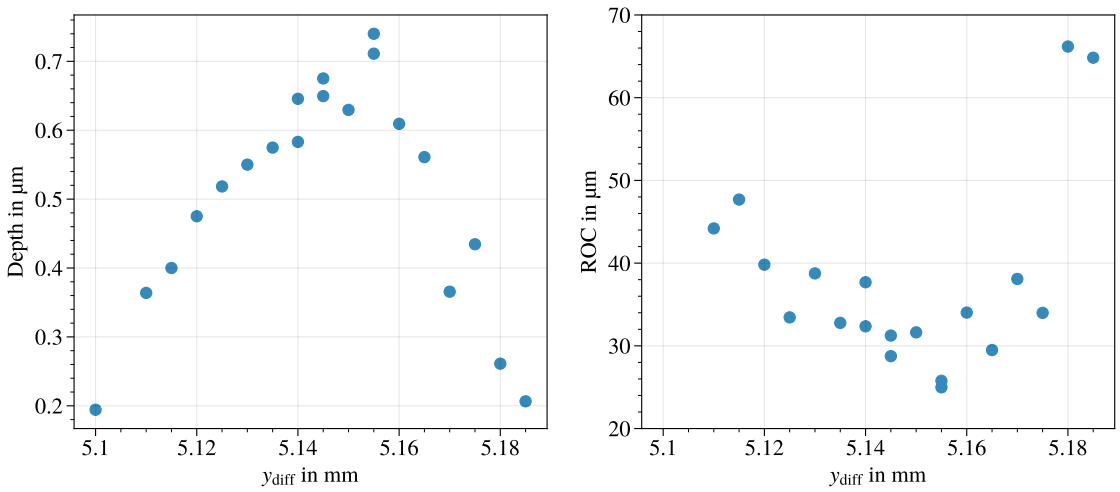

Figure 3.6: Plot of the dimple depth and radius of curvature as a function of the stage offset y_{diff} between the interferometric microscope and the laser. In the coordinate system of the 3D stage, the y-axis corresponds to the optical axis of the laser beam, meaning that the measurements show a sweep through the focus of the laser beam.

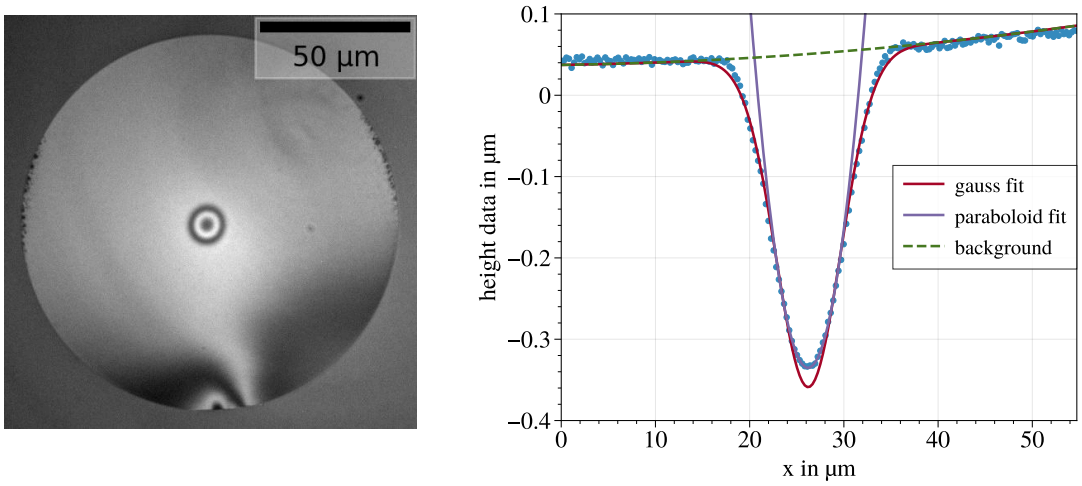

Figure 3.7: Interferometric microscope image of a laser-machined fiber end-face and reconstructed height profile along the x-axis with gaussian and paraboloid fits. This particular dimple exhibits a radius of curvature of $R = 44.4\,\mu\text{m}$ and a depth of $t = 0.39\,\mu\text{m}$.

the resulting dimple profiles, as shown in Figure 3.6. Since the machining is done at the same power and duration for all dimples in this measurement, the focus point is identified as the position where the depth is maximized and the radius of curvature is minimized, which we determined to be the case at $y_{\text{diff}} = 5.15\,\text{mm}$. This is necessary for achieving both a small radius of curvature and a shallow depth, both of which are important for the desired optical properties. By systematically controlling the laser machining parameters, specifically the pulse duration, pulse count and optical power, we can tune the resulting radius of curvature and dimple depth to our requirements. An example of a fiber that was laser-machined can be seen in Figure 3.7. The image shows a view of the fiber end-face taken with the interferometric microscope of the laser machining setup. The height profile is reconstructed from a series of these interferometric images taken automatically at predetermined offsets along the optical axis.

To determine the optimal parameters, we performed extensive testing on both planar glass substrates and optical fibers. We utilized planar substrates to efficiently test a large range of parameters, while the fiber tests included both polymer-coated *780HP* fibers and copper-coated *Cu800* fibers, which we later use in the final production run along with *Cu600* fibers. Since the latter two fiber types only differ in their core diameter, similar results were expected, which was later confirmed during the production run. The measurements, which are shown in Figure 3.8, demonstrate that the pulse duration significantly influences the dimple geometry. For each combination of pulse duration and pulse count, a range of dimples were produced using different laser powers, resulting in a range of depths

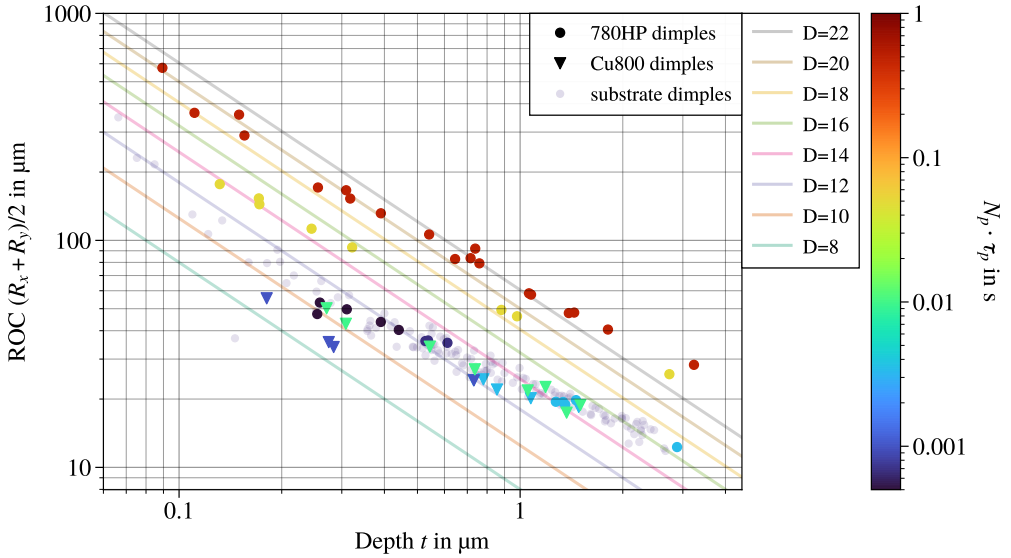

Figure 3.8: Radius of curvature plotted against dimple depth for different laser pulse durations τ_p and pulse counts N_p. Overall, a lower total pulse duration $N_\mathrm{p} \cdot \tau_\mathrm{p}$ results in a smaller figure of merit D. The substrate dimples are excluded from the color mapping, as they show no significant dependence on the pulse duration and are only kept as a reference.

and radii of curvature. Specifically, we found that shorter pulses result in a smaller radius of curvature and a shallower depth simultaneously, or a smaller usable diameter D, which is desired for our application. Both the *780HP* and the *Cu800* fibers provided comparable results, with the *Cu800* fibers showing slightly lower values of D at similar pulse durations. On the other hand, the dimples on substrates showed no significant dependence on the pulse count or total pulse duration, which can likely be attributed to the different thermal dissipation properties of the bulk substrate compared to the fibers. For the final production run, we utilized a single-pulse process with a pulse duration of 0.5 ms for the majority of the fibers, resulting in the dimple parameters shown in Figure 3.9.

The fraction of optical power that is coupled from the single-mode fiber into the cavity depends on multiple geometric factors, which are determined by the cavity design. In our transmission measurements, a coupling efficiency $\eta < 1$ only limits the absolute optical intensity circulating in the resonator, but does not influence the signal-to-noise ratio of the measurement. On the other hand, for reflection measurements, the uncoupled light is at least partly reflected back into the fiber and causes a background signal that can significantly decrease the signal contrast. When the beam leaves the fiber, the concave dimple on the end-face acts as lens, shifting the focus point of the fiber mode into the fiber itself, limiting the maximum possible coupling efficiency. The mode coupling efficiency

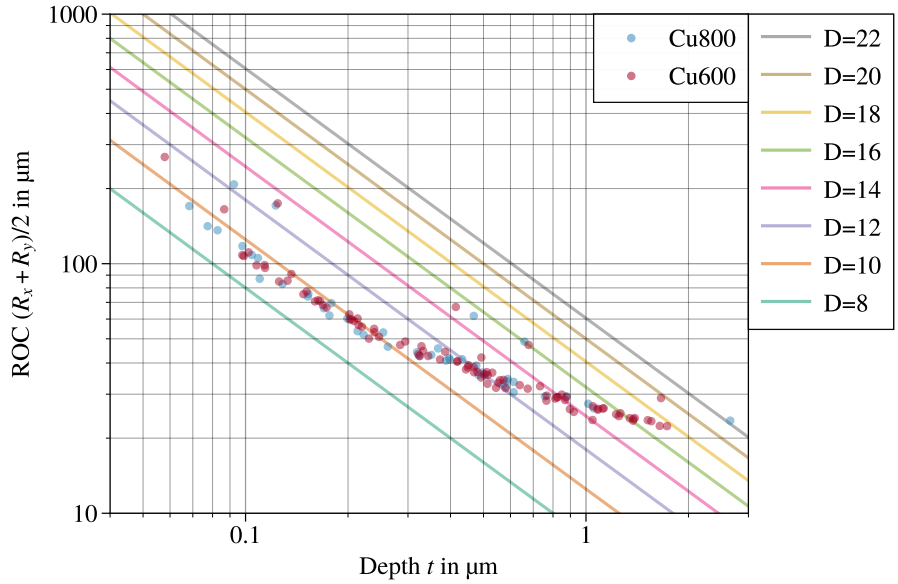

Figure 3.9: Average of the radius of curvature in x- and y-direction plotted against dimple depth for all 144 produced fibers contained in the coating run.

η can be described by calculating the overlap integral of the two Gaussian modes. The resulting coupling efficiency is given by: [18]

$$\eta = 4 \cdot \left(\left(\frac{w_\mathrm{m}}{w_\mathrm{f}} + \frac{w_\mathrm{f}}{w_\mathrm{m}} \right)^2 + \left(\frac{\pi w_\mathrm{f} w_\mathrm{m}}{\lambda} \right)^2 \left(\frac{1}{R_\mathrm{m}} - \frac{1}{R_\mathrm{f}} \right)^2 \right)^{-1} \tag{3.5}$$

where w_m is the cavity mode radius at the position of the curved mirror, w_f is mode field radius of the fiber and R_m is the radius of curvature of the fiber dimple. The effective radius of curvature of the fiber mode's wavefront after refraction at the fiber end-face is defined as $R_\mathrm{f} = -\frac{R_\mathrm{m}}{n_\mathrm{f}-1}$, where n_f is the refractive index of the fiber core. The theoretical coupling efficiency as a function of the normalized cavity length L/R is plotted in Figure 3.10 for different dimple radii. The coupling efficiency is reduced for smaller radii of curvature due to the stronger lensing effect and worsened mismatch between the wave fronts of the cavity mode and the fiber mode. This presents another tradeoff in the design of the cavity, since smaller radii of curvature are desirable for achieving smaller mode waists.

In addition to the axial wavefront matching, the coupling efficiency is also highly sensitive to radial offsets x_0 between the cavity mode and the fiber mode, causing an exponential decrease in coupling efficiency:

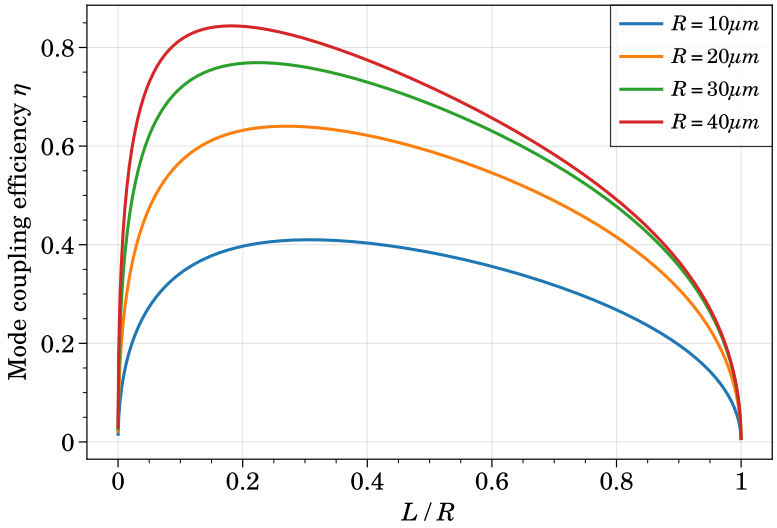

Figure 3.10: Calculated mode coupling efficiency between the cavity mode and the fiber mode as a function of the cavity length L for different values of the radius of curvature R (ROC) of the fiber mirror. For better visibility, the length is normalized to the ROC.

$$\begin{aligned} \alpha_{\text{offset}} &= \exp\left[-2\left(\frac{x_0}{\delta_{\text{off}}}\right)^2\right], \\ \text{with} \quad \delta_{\text{off}} &= \sqrt{\frac{\left(w_{0a}^2 + w_{0b}^2\right)^2 + (\lambda \Delta z/\pi)^2}{w_{0a}^2 + w_{0b}^2}} \end{aligned} \tag{3.6}$$

where w_{0a} and w_{0b} are the mode waists of the cavity mode and the fiber mode and Δz is the axial offset between the two modes [18]. Because of this, we need to position the dimple precisely at the position of the fiber core during the fabrication process. To achieve this high-precision alignment in the laser machining setup, we couple light into the end of the fiber, allowing us to easily see the position of the fiber core on the microscope of the setup, which is used for positioning. Since the fiber is single-mode, the core has a diameter of only about 5 µm for the *Cu600* fibers and 6 µm for the *Cu800* fibers, allowing for a very precise alignment. The distribution of offsets determined via parabolic fits to the height profiles of the dimples is shown in Figure 3.11 for all fibers contained in the coating run.

We determine the spatial misalignment between the fiber mode and the cavity mode by calculating the distance between the center of the interferometric microscope image and the origin of the paraboloid fitted to the dimple's height profile. Thereby, we determine

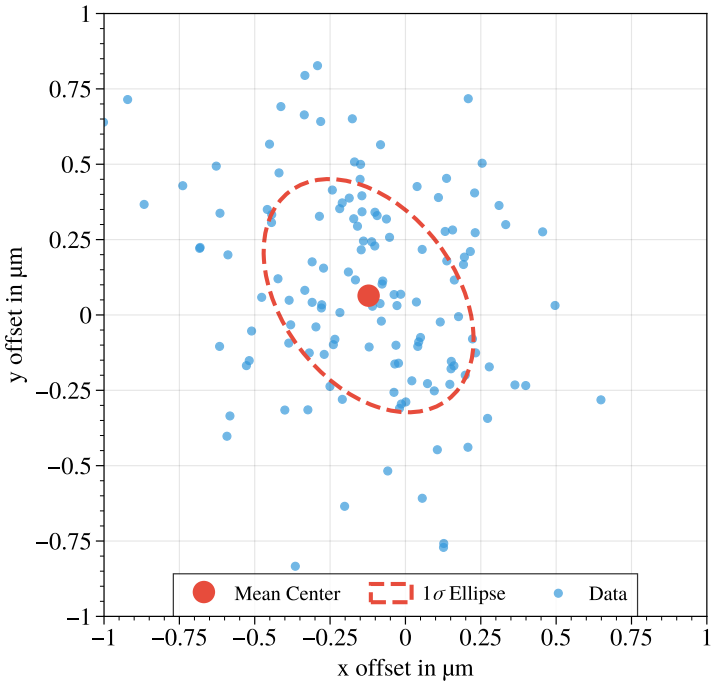

Figure 3.11: Measured radial offsets of the fiber dimples from the fiber core for all fibers contained in the coating run. The offsets are determined by the parabolic fits to the height profiles of the dimples. We obtain a mean offset of 0.14 µm with standard deviations of 0.43 µm and 0.29 µm along the main axes of the resulting ellipse, or a 0.51 µm standard distance of the absolute radial offset.

the offset to the expected position of the dimple. The distribution of these radial offsets is shown in Figure 3.11 for all fibers contained in the coating run.

We determine a mean radial offset of $\Delta\rho = 0.14\,\mu\text{m}$ with a 1σ standard distance of $0.51\,\mu\text{m}$. For example, in the case of a fiber dimple with a typical radius of curvature $R = 36\,\mu\text{m}$ and a radial offset of $0.56\,\mu\text{m}$, we get a factor α_{offset} between 0.934 and 0.957 depending on the cavity length at $\lambda = 760\,\text{nm}$.

3.4 Distributed Bragg reflector coating

Following the laser ablation process, we sent the fibers to the company *Laseroptik GmbH* for the application of the distributed Bragg reflector (DBR) coating. Once a high-reflectivity DBR coating is applied to these laser-machined fiber surfaces, along with the planar fused-silica substrates, we can obtain high finesse values necessary to reduce the cavity decay rate κ and to allow entering the strong coupling regime. Securing the fibers for the

coating process is made possible by the custom fibers holders (see Figure 3.12), which are in use in the Fiberlab. These individual holders are mounted into a so-called coating disk, which can be inserted into the coating machine by the company. For this specific coating run, we adapted the design of the coating disk to accommodate six fiber holders, allowing us to have a total of 144 prepared fibers coated simultaneously. The disk also accommodates two fused silica wafers with a 100 mm diameter, which serve as planar cavity mirrors once cut to size (see Figure 3.12).

During the coating process, the long ends of the optical fibers must be securely contained to prevent them from hanging loosely into the coating chamber, which could damage them, as the coating disk rotates at around 120 revolutions per minute during the coating process. To solve this issue, we designed custom aluminum enclosures that attach directly to the rear of each fiber holder, allowing us to coil up the excess length of each fiber and contain it within the box, resulting in a neatly organized assembly. These custom aluminum fiber boxes were manufactured by the mechanical workshop of the Physical Institute.

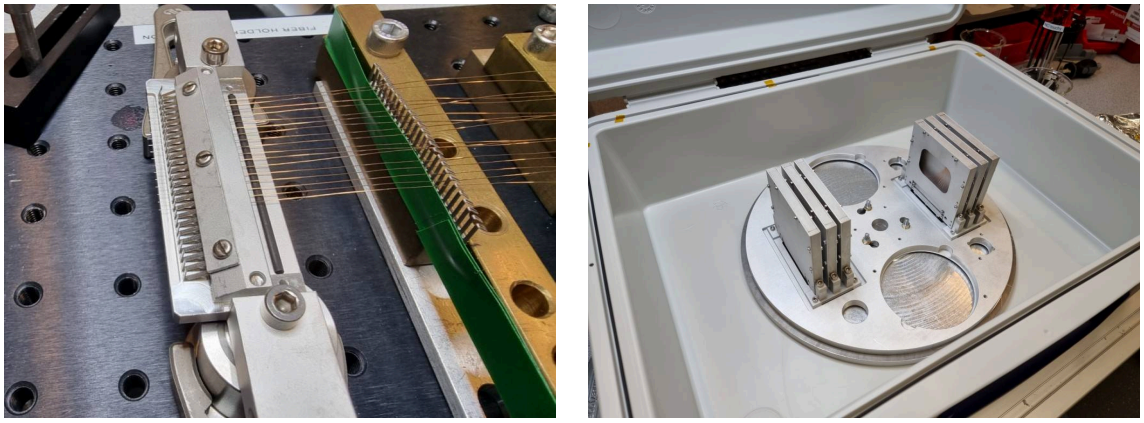

Figure 3.12: Photographs of fiber processing equipment. **Left:** Fiber holder used to mount the fibers during the laser ablation process and coating, partially filled with fibers. The fibers are pushed down into the grooves by the thin metal fingers, and are firmly secured by an additional bar at the back of the holder once all fibers are inserted. This type of holder is commonly used in the Fiberlab. **Right:** The coating disk assembly, ready to be sent for coating to *Laseroptik GmbH*, with six holders mounted to the disk. The long ends of the fibers are coiled up and contained within custom aluminum boxes attached to the back of each holder, preventing them from hanging loosely into the coating chamber during the coating process. The disk also has two spaces for mounting 100 mm diameter fused silica wafers.

3.5 Validation of strong coupling parameters

To evaluate the suitability of the fabricated dimple geometries for reaching the strong coupling regime, the relevant coherent exchange rate g and decay rates κ and γ are calculated as a function of the absolute cavity length L. An example of this evaluation is shown in Figure 3.13 for a set of dimple parameters ($R = 36.00\,\mu\text{m}$, $D = 13.15\,\mu\text{m}$) that is present in the range of our fabricated fibers. The cavity photon decay rate κ was calculated using a cavity finesse of $\mathcal{F} \approx 3000$, which is the expected value for our DBR coatings at this specific wavelength. For the exciton decay rate γ, we consider the typical values reported in literature for $MoSe_2$ and WSe_2 monolayers encapsulated in hBN. Encapsulating the monolayer in hexagonal boron nitride (hBN) at cryogenic temperatures suppresses inhomogeneous broadening present in bare monolayers. Under these conditions, the exciton linewidths in $MoSe_2$ and WSe_2 monolayers reach limits of approximately 1.5 meV to 4 meV [19–21]. We assume a representative exciton decay rate of $\gamma \approx 2\,\text{meV}$ for the theoretical evaluation in Figure 3.13.

We find that at the minimum cavity length L_{min}, the calculated coupling strength g exceeds the exciton decay rate γ by approximately one order of magnitude, while the cavity photon decay rate κ is about two orders of magnitude smaller than g, satisfying

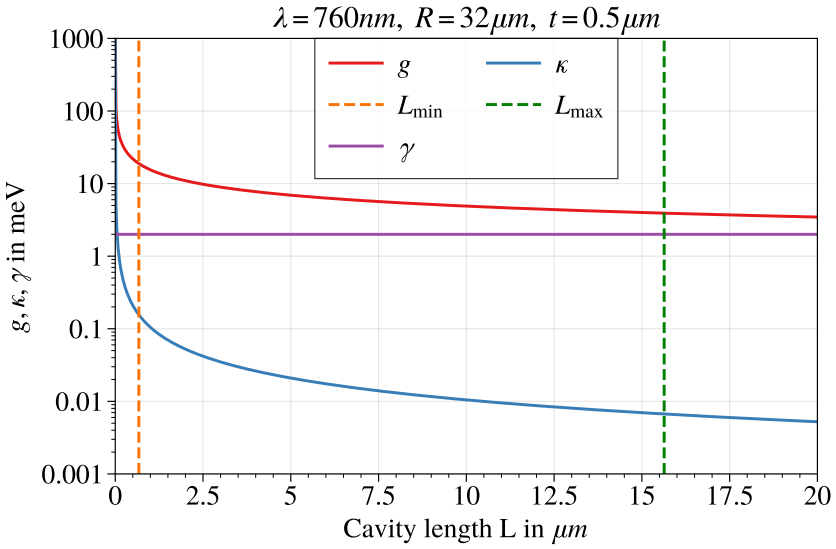

Figure 3.13: Calculated coupling and decay rates as a function of the cavity length L for a representative fabricated fiber ($R = 32\,\mu\text{m}$, $t = 0.5\,\mu\text{m}$) at a wavelength $\lambda = 760\,\text{nm}$. The physically accessible cavity length is limited by L_{min} and L_{max}. Within this accessible regime, the coherent exchange rate g clearly dominates both the cavity photon decay rate κ and the exciton decay rate γ, fulfilling the condition for the strong coupling regime ($g > \kappa, \gamma$).

the condition for the strong coupling regime ($g > \kappa, \gamma$). This confirms that the concave fiber mirrors produced by us satisfy the geometric and optical requirements necessary to observe exciton-polaritons.

In summary, we established and applied a routine for the fabrication of fiber mirrors for a fiber-based microcavity that is specifically designed for strong coupling experiments. By optimizing the chemical preparation and CO_2 laser ablation parameters, we successfully modified 144 fiber end-faces to feature concave dimples with a range of different parameters. Finally, a custom high-reflectivity DBR coating was applied to the fibers and two planar fused silica substrates by an external company.

CHAPTER 4

Cavity implementation

To achieve strong coupling of cavity photons to excitons, we need to maximize light-matter interactions while minimizing mechanical vibrations and thermal broadening of the exciton resonance. This requires a stable, high-finesse microcavity capable of operating at cryogenic temperatures. The experimental setup must allow for precise tuning of both the spatial position on the sample and the absolute cavity length: We need to accurately position the cavity mode onto the 2D material sample to locate the TMD monolayer. Simultaneously, precise control of the cavity length on the order of nanometers is required to tune the resonance to the exciton energy and to systematically scan the detuning. Integrating these optical and mechanical components into our liquid-helium cryostat requires a custom-built assembly that ensures both mechanical stability and precise optical alignment at cryogenic temperatures. We initially characterized the cavity configuration and the viability of the processed fibers and reflective coatings on a more accessible, ambient-temperature testing setup before moving to the final cryogenic assembly.

4.1 Microcavity testing setup

Before integrating the cavity into a cryogenic setup, we implemented a testing setup to characterize the cavity performance and to verify the functionality of the processed fibers and coatings. The purpose of the testing setup was to implement a fiber-based microcavity in an accessible configuration that allows us to modify various degrees of freedom. At its core, the testing setup consists of a 3-axis translation stage (Thorlabs Nanomax) with piezo actuators, that holds the cavity fiber, and a mirror mount holding the coated planar substrate, as shown in Figure 4.1. For these ambient tests, we utilized one of our previously processed and coated fibers (number J3-6), which is a fiber of the type *Cu600*. The laser-

machined dimple on this fiber has a depth of $t = 0.42\,\mu\text{m}$. Due to a slight asymmetry during the ablation process, it exhibits a slightly elliptical profile with radii of curvature of $R_x = 38.4\,\mu\text{m}$ and $R_y = 42.7\,\mu\text{m}$, resulting in an average usable diameter of $D = 11.7\,\mu\text{m}$. We mounted the $10\,\text{mm} \times 10\,\text{mm} \times 0.5\,\text{mm}$ substrate in the mirror mount by glueing it to a 1 inch post spacer disk with a hole in the middle using epoxy adhesive. This adjustable mount allows us to tune the angle between the planar substrate and the optical fiber.

For both the ambient testing setup and the subsequent cryogenic cavity scanner, we utilize planar substrates with a different DBR coating (coating B-12752-02) than our cavity fibers (coating B-12752-03). These substrates feature a significantly higher intensity transmission of approximately 2000 ppm, compared to the 300 ppm transmission of our newly coated cavity fibers. We deliberately implemented this asymmetric coating configuration to lower the overall cavity finesse, which broadens the resonance linewidth and significantly simplifies locating the spectral cavity resonances compared to a symmetric configuration.

The translation stage enables tuning of the cavity length as well as adjusting the lateral position of the fiber relative to the substrate. Behind the substrate, we mount an aspheric lens (*Thorlabs A397TM-B*, $f = 11\,\text{mm}$) in an adjustable lens tube for collimating the light transmitted through the cavity.

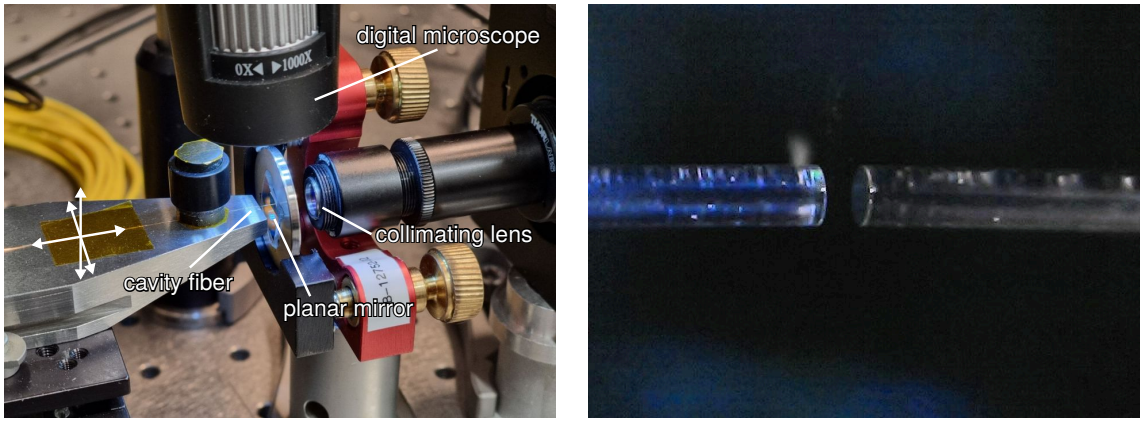

Figure 4.1: **Left:** Close-up photograph of the microcavity testing setup. The cavity fiber is secured on a 3-axis translation stage for fine-tuning the cavity length and lateral position. The coated planar substrate is held in a mirror mount, which allows us to adjust the angle between the substrate and the fiber. Behind the substrate, a collimating lens is housed in an adjustable lens tube. **Right:** Microscope image of the cavity fiber positioned directly in front of the planar mirror substrate with its reflection visible on the substrate. The image was taken with the digital microscope positioned above the setup.

Coupling light through the fiber and measuring the reflection is the simplest method for acquiring a cavity signal without requiring any alignment other than the alignment of the fiber to the substrate. However, suboptimal coupling efficiency leads to strong back-reflections into the fiber, resulting in poor signal contrast. We therefore add the option to measure the cavity transmission to achieve better contrast. The cavity substrate is adjusted to be approximately perpendicular to the cavity fiber to ensure an optically stable resonator configuration. Further alignment is done by maximizing the signal of the longitudinal cavity resonances, which is is proportional to the intensity circulating in the cavity mode. Measuring the transmission signal is done by sweeping the cavity length via the piezo in the translation stage and recording the cavity response either in transmission using a photodiode behind the collimating lens or by using a fiber splitter to extract the light reflected back into the cavity fiber.

In order to be able to analyze the cavity transmission using a spectrometer, we need to couple the transmitted cavity signal into a collection fiber. As mentioned above, utilizing the transmission signal is preferred because it provides a significantly higher contrast ratio than the reflection signal. However, optimizing this fiber coupling is challenging due to the low transmitted optical power caused by the cavity drifting out of resonance quite quickly. To facilitate the alignment, a non-polarizing beam splitter cube directs a part of the collimated cavity mode onto a camera, while the transmitted part travels toward the collection fiber (see Figure 4.2). First, we send laser light backwards through the collection fiber. We then place an alignment mirror on the remaining side of the beam splitter and adjust it until the light reflects back into the fiber, creating a perfectly aligned reference beam. Since the reference beam and the part of the beam that is reflected by the cavity substrate originate from the same point on the beam splitter, the two beams are parallel if their spots overlap on the camera, resulting in the beam reflected from the cavity substrate being coupled back into the collection fiber as well. Bringing the two spots together requires an iterative approach of adjusting either of the two mirrors in front of the collection fiber and readjusting the alignment mirror to ensure maximal coupling back into the fiber.

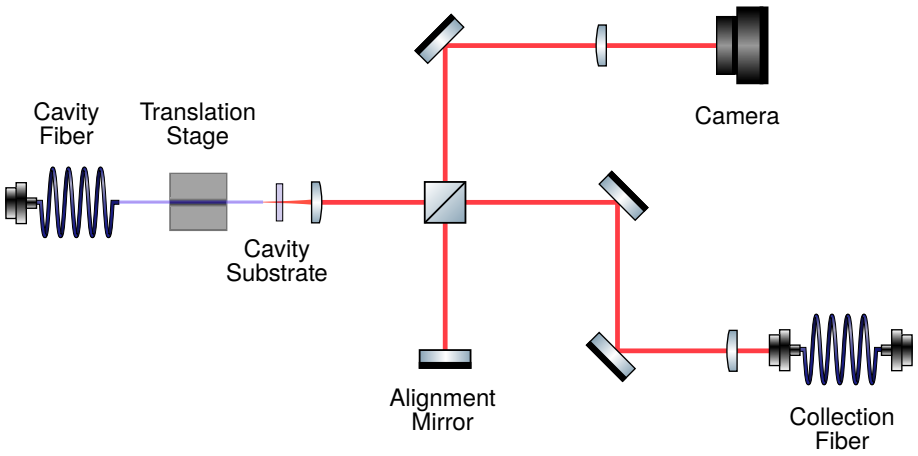

Figure 4.2: Schematic of the optical setup for the microcavity testing setup.

4.2 Cavity Setup for cryogenic measurements

Making the step to a cavity setup that can operate at cryogenic temperatures requires the integration of all functionalities present in the testing setup into a volume small enough to fit into the dipstick of the cryostat. We adapted our design from an earlier version by the group of Professor Ataç İmamoğlu at ETH Zürich. In this implementation, the assembly is housed in a titanium cylinder (48.5 mm in diameter and 83 mm in height), as shown in Figure 4.3. We call this assembly the "cavity scanner", due to the ability to scan the cavity mode across the sample by moving the substrate in the xy-plane, while tuning the cavity length via the z-positioner. Collecting the transmission signal from the cavity through the substrate is made possible by mounting the substrate with its coated side and TMD sample facing down and the fiber facing upwards. The assembly contains three high-precision attocube positioners: a stack of two horizontal positioners (`ANPx101/RES/LT`) allow us to position the sample laterally to the fiber, while a vertical positioner (`ANPz102/RES/LT`) is used for tuning the cavity length. Moving only the substrate in the xy-plane has the advantage of the mode waist always staying at the same position, retaining optical alignment. To perform the measurements under the best possible conditions, we installed a previously unused fiber (number J4-11) into the assembly. The dimple on this new fiber features a depth of $t = 0.54\,\mu\text{m}$ and radii of curvature $R_x = 30.3\,\mu\text{m}$ and $R_y = 33.3\,\mu\text{m}$, resulting in an average usable diameter of $D = 11.7\,\mu\text{m}$.

The cavity scanner is made up of a cylindrical base and a lid, which are attached to each with four screws, allowing us to more easily access the interior of the cylinder for mounting the positioners, the sample and the fiber. Three $\varnothing 6\,\text{mm}$ cage rods are attached to the lid for mounting the assembly to the dipstick insert of the cryostat. The lid also

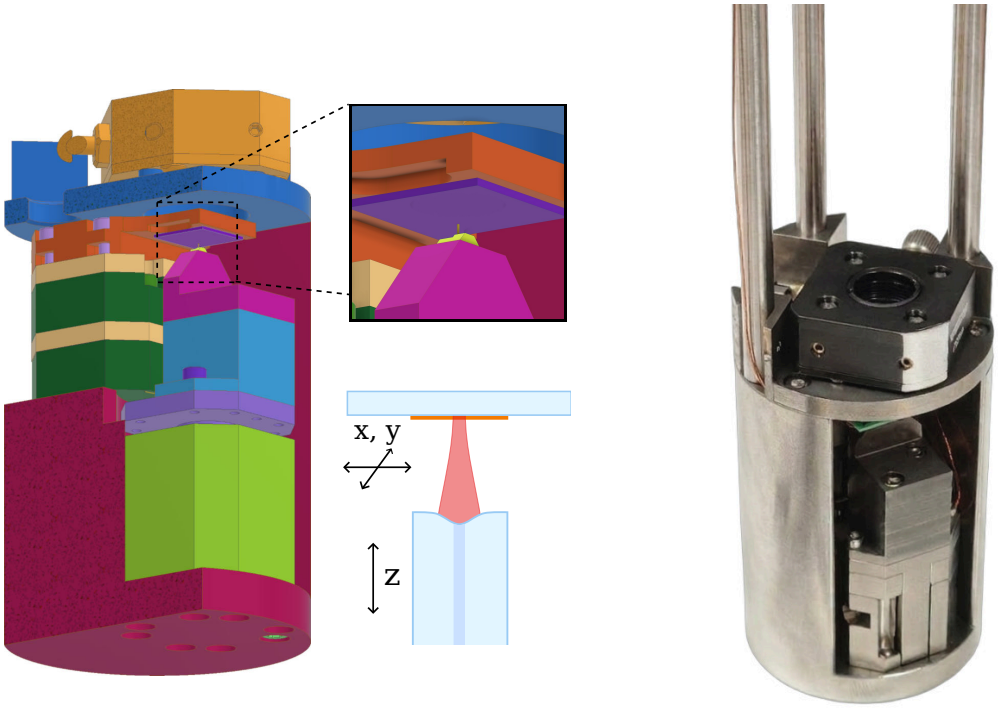

Figure 4.3: **Left:** Cross-section view of the cavity assembly for cryogenic measurements. The sample is mounted onto the sample holder (orange) facing downwards, which in turn is mounted to the x- and y positioners (dark green). The fiber is seated in the L-shaped mount (pink) on top of the z-positioner, pointing up. **Right:** Photograph of the cavity assembly for cryogenic measurements

incorporates a lens mounted on a translation mount, which can be slid up and down along rods on the lid, allowing for precise adjustment of the focal distance to accurately collimate the transmitted light. In order to make translation mount fit inside the footprint of the assembly, we had to file down one of its corners to match the curvature of the cylinder.

Once the microcavity assembly is sealed within the cryostat, we no longer have a way to visually estimating the cavity length or the sample position. Consequently, the alignment of the fiber relative to the planar mirror must be performed blindly, relying exclusively on the optical transmission signal. This poses a challenge when approaching the fiber towards the substrate, as moving the z-positioner beyond the point of mechanical contact could easily damage the fiber or the sample. For the initial coarse adjustment of the cavity length, we rely on the coordinate readout of the z-positioner. As the z-coordinate of mechanical contact between fiber and substrate is only known at room temperature, once the assembly is inserted into the cryostat, we initially move the z-positioner to a safe distance about 1 mm below the room temperature contact position. Once we reach this position, mono-

chromatic laser light is coupled into the cavity while the cavity transmission is monitored using a camera. As we slowly move the z-positioner further up, the appearance of cavity modes on the camera clearly indicates that the cavity length has reached the stability range of the resonator. In fact, we were able to observe faint interference fringes on the camera even before reaching stable resonator modes, which can act as an additional indicator for the proximity to the substrate. Once these stable modes are visible, the light source is switched to a broad-spectrum white light source (*Thorlabs SLS201L/M*) for determining the absolute cavity length from the transmission spectrum, as described in Section 4.3. Precise positioning of the sample relative to the fiber is then achieved by recording a raster scan of the cavity transmission over the sample, as described in Chapter 5.

4.3 Finesse measurements

The performance of the cavity can be characterized by its finesse $\mathcal{F}$, which describes the ratio of the free spectral range to the full width at half maximum of the transmission peaks. In this section, the methods used for measuring the finesse and its dependence on the cavity are described.

The simplest approach would be to extract the finesse directly from the cavity transmission spectra, but at the finesse values around 3000 that we target, this is unfeasible, as the linewidth of the cavity resonances falls below the optical resolution limit of our spectrometer. To overcome this limitation, we combine two measurement methods to separately determine the cavity finesse and the corresponding cavity length. The finesse itself is measured by coupling monochromatic laser light at approximately 760 nm into the cavity and scanning the cavity length using the z-positioner. The transmitted intensity is recorded using a photodiode and an oscilloscope, enabling a precise measurement of the resonance linewidths where the effective resolution is determined by the modulation speed of the cavity length and by the bandwidth of the electronics. In addition to this length-scan measurement, we perform a second measurement step where a broad-spectrum white light source is coupled into the cavity to record transmission spectra at a fixed cavity length using a spectrometer. These spectra allow us to determine the absolute cavity length as well as the longitudinal mode orders from the spacing of the resonance frequencies.

When extracting the absolute cavity length and the mode orders from these spectra, it is necessary to account for the wavelength-dependent phase shift and resulting group delay of the DBR mirrors [16], as discussed in Section 2.3. The effective optical path length, which affects the resonance condition, differs from the physical mirror separation due to the phase shift upon reflection φ_{DBR}. Additionally, the modal penetration depth L_D modifies the Gouy phase shift, which in turn alters the resonance condition according to

Equation (2.13). Taking these penetration depths into account is important for accurately assigning the measured finesse values to the corresponding optical cavity lengths.

To extract the absolute length from the white light spectra, we first assign relative mode orders to the observed transmission peaks. Following the formula for the resonance frequencies in Equation (2.10), the relationship between the resonance wavelength λ and its corresponding longitudinal mode order $m(\lambda)$ can be expressed as:

$$m(\lambda) = \frac{2L}{\lambda} + \frac{\varphi_{\mathrm{DBR}}(\lambda)}{2\pi} - \frac{1}{\pi}\Delta\zeta \tag{4.1}$$

By fitting this function to the counted relative mode orders as a function of the measured resonance wavelengths, we can determine the absolute cavity length L. An example of this fitting procedure is illustrated in Figure 4.4.

Once the absolute cavity length is known for a specific reference spectrum, we determine the finesse by performing a length scan of the cavity. For this measurement, we couple a monochromatic laser at a wavelength of approximately 770 nm into the cavity and record the transmitted intensity. We perform this scan by modulating the DC voltage applied to the piezo of the positioner, rather than stepping the positioner, as stepping introduces unpredictable movement that is difficult to model. As the cavity length crosses

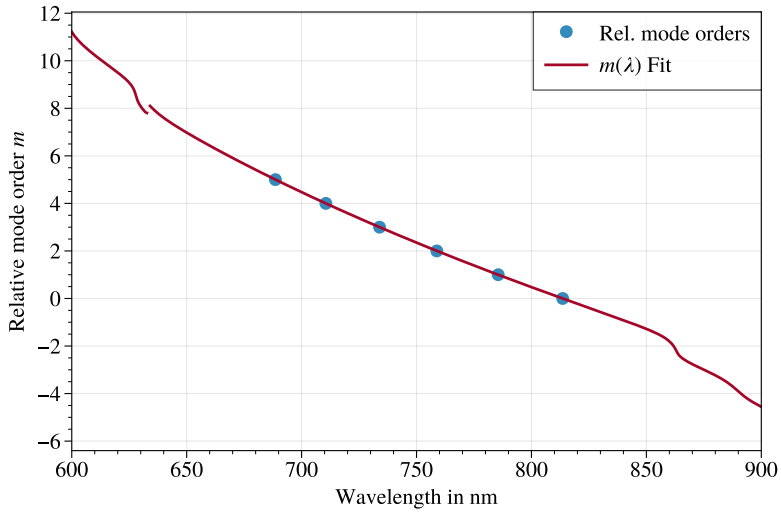

Figure 4.4: Example for determining the absolute cavity length from a transmission spectrum. The relative longitudinal mode orders, counted from an arbitrary reference mode, are plotted against the corresponding resonance frequencies. The fit takes into account the wavelength-dependent phase shift of the DBR mirrors and the resulting group delay. The discontinuity in the curve at $\lambda = 633\,\mathrm{nm}$ arises from the jump of the mirror phase shift (see Figure A.1).

resonant points, we observe transmission peaks using a photodiode and an oscilloscope. We calculate the finesse by comparing the spacing of these peaks to their widths. Because the positioner's movement is non-linear with respect to time, we must first calibrate the x-axis of the length scan to properly evaluate the data. Using the information collected using the spectrometer, we can directly convert the time axis of the oscilloscope data to a cavity-length-axis: By comparing the peaks in the length-scan data with the peaks in the reference spectrum, we can assign mode orders and absolute lengths to the length-scan peaks by rearranging Equation (2.10):

$$L_{mpq} = \frac{\lambda}{2}\left(m - \frac{1}{2\pi}(\varphi_{\mathrm{DBR}}(\omega) + 2(p+q+1)\Delta\zeta)\right) \tag{4.2}$$

Since the Gouy phase shift $\Delta\zeta = \arcsin\left(\sqrt{L/R}\right)$ also depends on L, the equation must be solved numerically. Specifically, the first transmission peak observed in the length scan corresponds to the resonance peak located to the right of the laser wavelength in the reference spectrum, since we begin the length scan at the same length the spectrum was recorded at and subsequently shorten the length: As the cavity length decreases, the resonances shift towards shorter wavelengths, causing the mode that was initially at a longer wavelength to sweep across the wavelength of the laser. We then apply a polynomial fit to these discrete points to create a continuous mapping from time to cavity length, as shown in Figure 4.5.

At cryogenic temperatures, the expansion of the piezo positioners we can achieve by applying a DC voltage is drastically reduced compared to room temperature, with only two longitudinal modes visible over the scan range. Because two data points are insufficient to accurately fit a non-linear calibration curve, we have to rely on transverse modes to act as additional reference points. Specifically, we use the $(n, 2, 0)$ and $(n, 0, 2)$ modes, which appear visibly split in the transmission spectrum (see Figure 4.6) due to a slight asymmetry in the laser-machined fiber dimple, caused two different radii of curvature along the main axes of the elliptical dimple leading to a difference in the Gouy-phase term in Equation (2.10). Since these higher-order modes get spatially filtered by the coupling into the collection fiber, they are only visible at high amplifications of the photodiode signal, which introduces a lower bandwidth and can falsify the measured peak widths. Because of this, our measurement requires two consecutive length scans: A scan at high amplification allows us to find the positions of the transverse side modes and establish the non-linear calibration. Subsequently, a second scan is recorded at a lower gain setting to accurately determine the natural linewidths of the fundamental modes for the actual finesse calculation. The finesse can then be calculated as the ratio between peak spacing and peak width. A plot showing how these values are determined can be found in Figure 4.7

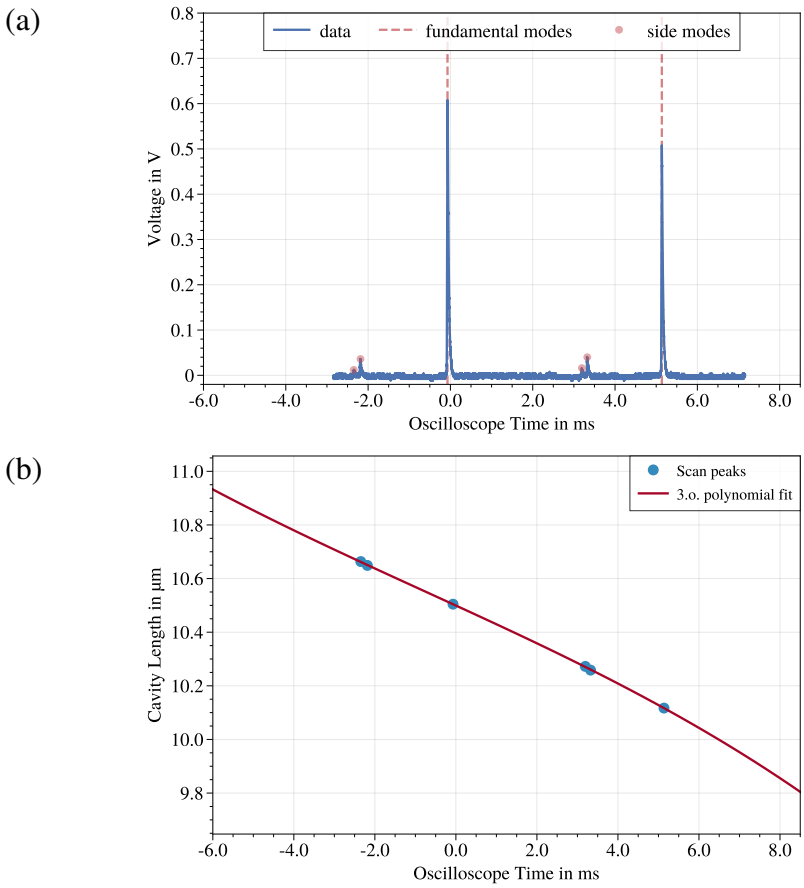

Figure 4.5: Example for a length scan calibration at cryogenic temperatures, mapping the oscilloscope time axis to the absolute cavity length in order to correct for non-linear movement of the z-positioner. **(a)** Raw oscilloscope trace of the cavity transmission signal. **(b)** Polynomial fit to the absolute cavity lengths calculated for the specific mode orders. The resulting transmission peaks exhibit a structural asymmetry, which is caused by the limited electronic bandwidth of the photodiode at the high gain settings necessary for resolving the transverse modes. In the following finesse calculations, we use data recorded at lower gain.

We measured the cavity finesse using both the ambient testing setup and the cryogenic cavity scanner, with the results compared in Figure 4.8. The cavity scanner yields a consistently higher finesse across the measurement range. The maximum theoretical expected finesse is 2894 for the testing setup and 3109 for the cavity scanner. This difference in the expected values arises because the respective length scans were performed at slightly different laser wavelengths, resulting in different DBR reflectivity values. We attribute the overall lower measured finesse of the testing setup to increased mechanical vibrations in the ambient environment. If these vibrations occur on a faster timescale than the

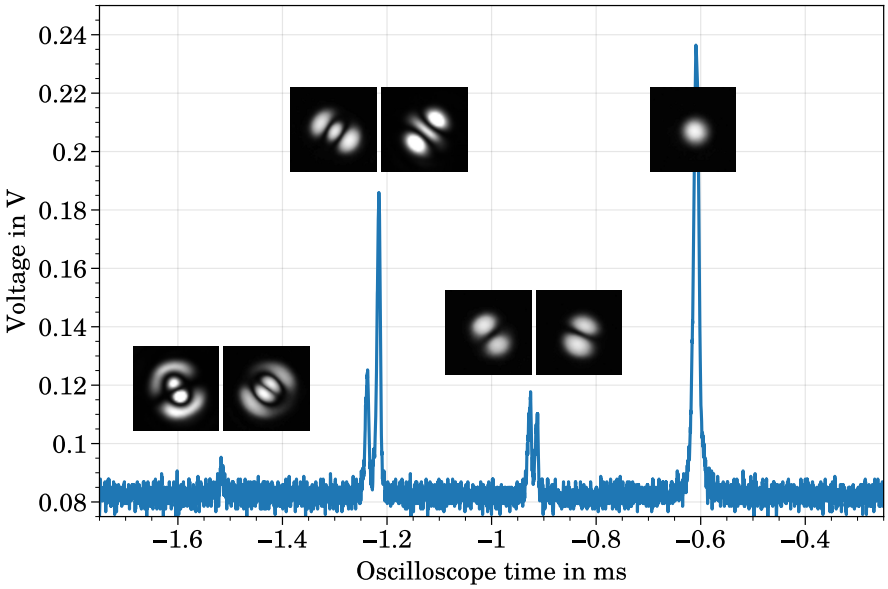

Figure 4.6: The cavity transmission during a length scan as recorded on the oscilloscope. We see a single fundamental longitudinal mode to the right, as well as several transverse side modes. The splitting of the side modes results from a slight asymmetry of the fiber dimple. The overlaid mode profiles were recorded separately by manually tuning the cavity length.

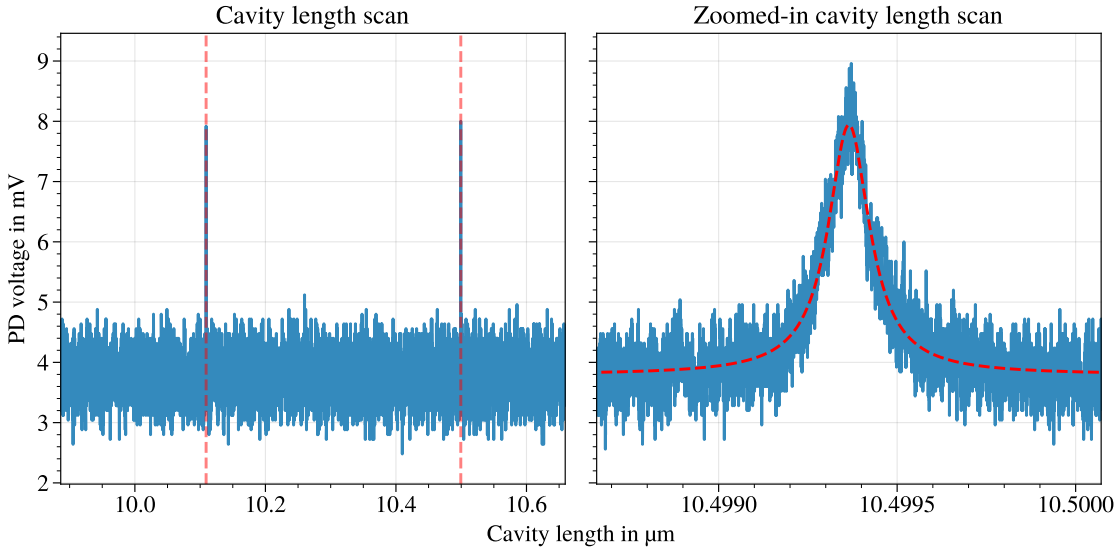

Figure 4.7: Example for a finesse measurement using a length scan. The peak spacing is determined in the broader scan, while the individual peak widths are determined in a separate, zoomed-in measurement.

measurement speed of the length-scan, they could broaden the transmission signal peaks. The cavity scanner provides a more mechanically stable configuration due to its compact, robust design and the short length of the fiber end that extends out from the holder. Notably, the measurements also reveal a significant, length-dependent decrease in finesse even before the expected decrease. We hypothesize that this is caused by higher intra-cavity losses at larger beam diameters due to contamination of the substrate. As the cavity length L is increased, the transverse mode profile expands on the planar substrate, meaning that a larger area of the mirror is sampled by the cavity field. While the majority of the measurements fall below the theoretical limit, the two data points exceeding the expected finesse can likely be attributed to an error introduced by the length scan calibration.

During the respective finesse measurement series, we reached a minimum cavity length of 2.34 µm for the room-temperature test cavity and 2.36 µm for the cryogenic cavity scanner. Based on the geometric profiles of the specific fiber mirrors used in each setup, the theoretical minimum lengths are calculated to be 0.59 µm and 0.71 µm, respectively. We deliberately chose not to push the systems to these absolute theoretical

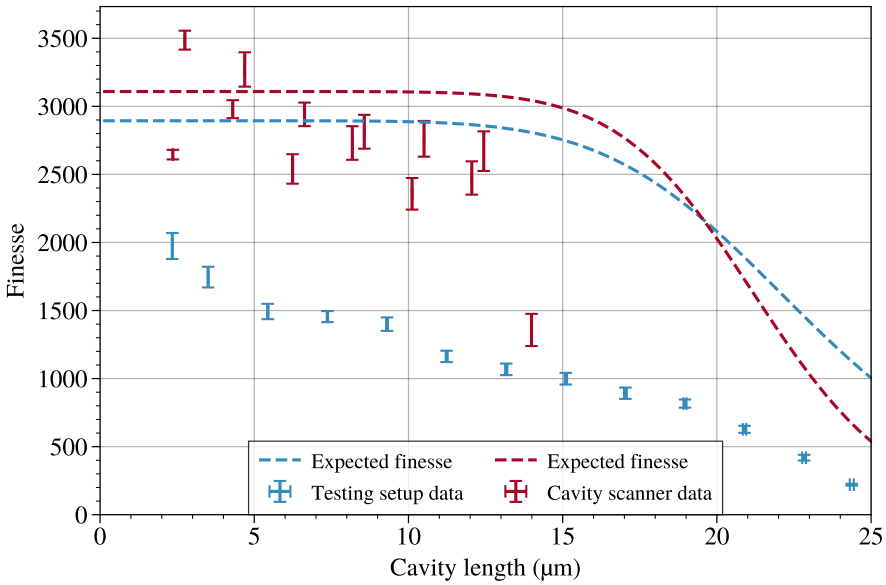

Figure 4.8: Comparison of measured finesse values at different cavity lengths for the ambient testing setup and the cryogenic cavity scanner. The dashed lines indicate the theoretical expected finesse values considering clipping losses at the outer regions of the fiber dimple. The larger uncertainty for the cavity scanner data arises from the less accurate length scan calibration at cryogenic temperatures. We attribute the lower overall measured finesse of the testing setup to increased mechanical vibrations.

limits to prevent damage to the fragile fibers. However, as theoretically demonstrated in Figure 3.13, operating the cavity at a length of approximately 2.3 µm already satisfies the strong coupling condition.

CHAPTER 5

Integration of a 2D material stack

To investigate exciton-polaritons within the microcavity, we integrate a two-dimensional transition metal dichalcogenide (TMD) monolayer into the resonator. We fabricate the 2D material stack using a specialized transfer setup, allowing us to create structures that fit the specific requirements of our experiments.

5.1 Sample fabrication

Before the transfer of the 2D material stack, we prepare a DBR-coated fused silica substrate with gold structures, which include eight pads for wirebonding and gold traces leading to the center (see Figure 5.1). The first step to creating the contact structures is to spin-coat the sample with a layer of PMMA resist followed by a layer of *Electa 94* to ensure electrical conductivity across the sample surface, which is crucial for electron beam lithography. We then fabricate the structures using electron beam lithography and subsequent physical vapor deposition of 5 nm of chromium, followed by an 80 nm layer of gold using thermal evaporation, where the chromium acts as an interface layer to improve the adhesion of the gold to the substrate. After evaporation, the chromium and gold in the undeveloped areas is lifted off by submerging the sample in N-methyl-2-pyrrolidone (NMP) at 80 °C for several hours, leaving only the desired gold structures on the sample. In the center, a square area with a side length of 150 µm is left free for the 2D material stack. Creating the initial gold structures before the transfer of the 2D material stack is essential for the precise alignment of the stack with the contact structures, since locating the stack directly using the scanning electron microscope (SEM) would cause an unwanted exposure of the resist. This initial pattern also includes alignment markers which are used in the second lithography step.

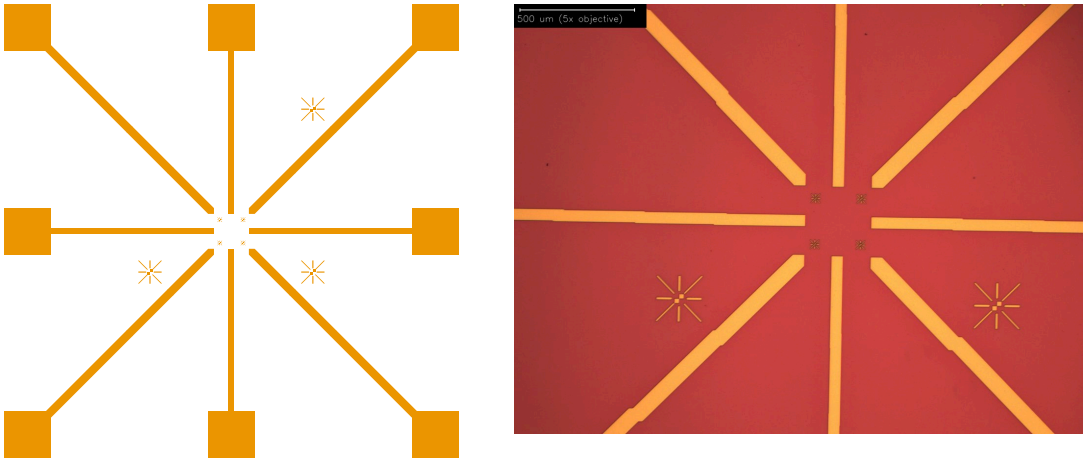

Figure 5.1: Design and lithography result of the initial gold contact structures on the DBR-coated substrate. **Left:** Schematic layout containing the large outer wirebonding pads and the geometric markers required for aligning the subsequent lithography step. The entire area is about 4 mm wide. **Right:** Optical microscope image of the corresponding fabricated gold structures prior to the integration of the 2D material stack.

We begin the fabrication process of a 2D material stack with the mechanical exfoliation of bulk crystals using sticky tape to repeatedly peel off crystal layers. The resulting crystal flakes are transferred onto silicon wafers and are automatically searched for suitable thin flakes using a custom optical microscope setup. This automated system also determines the thickness of the individual flakes by comparing their reflective properties with calibrated values. This allows us to accurately distinguish monolayers and determine the thickness of hBN flakes with an accuracy of 5 nm. We utilize these measured thickness values to select hBN flakes that match the requirements of our microcavity field distribution. After selecting these suitable flakes, we trace their outlines in software to create a stacking plan by positioning these outlines relative to each other. A traced stacking plan can be seen in Figure 5.2. Our 2D material stacks typically consist of a TMD monolayer encapsulated between two flakes of hexagonal boron nitride (hBN), a graphite contact flake to the monolayer and a graphite back gate for inducing charge carriers on the monolayer. Optionally, a graphite top gate can be added, if the experiment targets exciton confinement. We use a graphite flake for the contact to the TMD monolayer instead of a direct gold contact to be able to entirely encapsulate the fragile monolayer and to reduce the risk of damaging it.

The stacking plan has to take certain factors into account, like the overlap of the flakes, as we want to encapsulate the TMD monolayer between two hBN flakes and prevent any unwanted electrical contact. Additionally, the contact should cover enough area of the

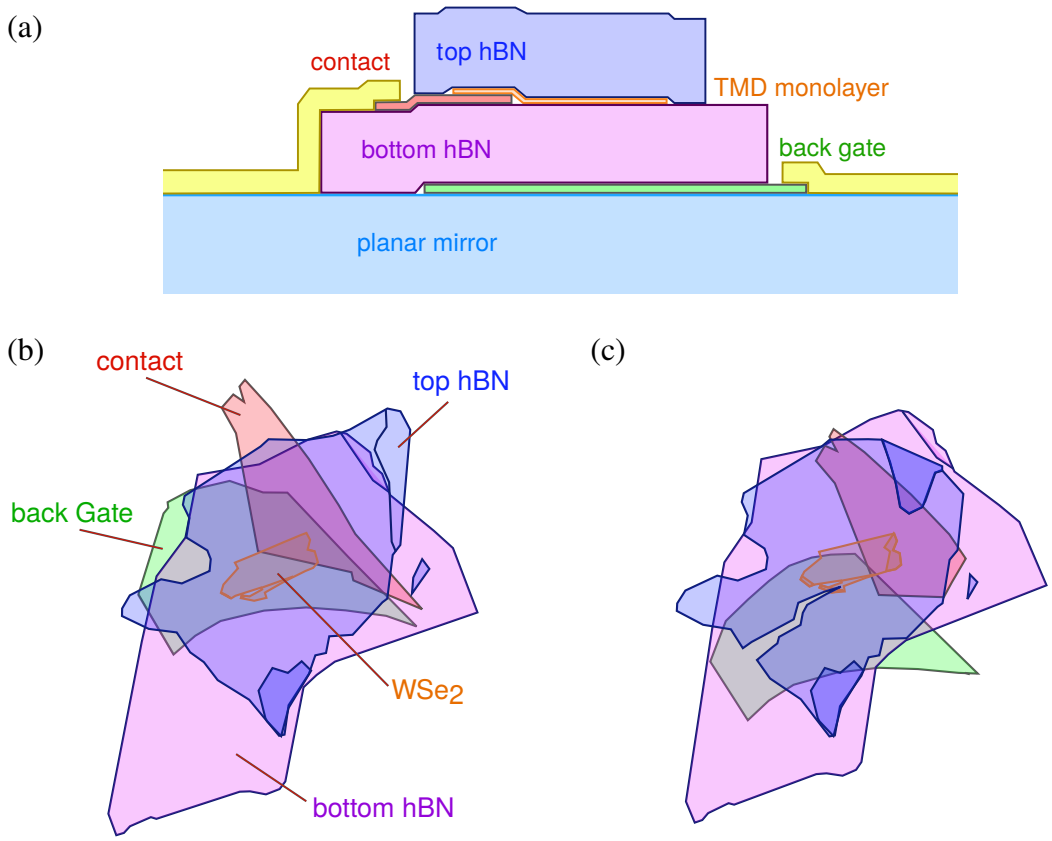

Figure 5.2: **(a)** Side profile of the 2D material stack. **(b)** Stacking plan for the sample. **(c)** Traced sample after transfer onto the mirror and second lithography step.

monolayer to ensure good electrical contact, while still leaving enough area of the monolayer uncovered for optical access. For the physical assembly of the 2D material stack, we utilize a polydimethylsiloxane (PDMS) stamp coated with a thin polycarbonate (PC) film to pick up and stack the individual flakes. Once complete, the stack is deposited onto the DBR-coated fused silica substrate that will act as the planar cavity mirror. Following the successful transfer of the complete stack onto the DBR-coated substrate, the graphite contact and backgate flakes are electrically contacted with gold structures customized to the specific geometry of the stack, which we apply in a second lithography step. In preparation for this step, we spin-coat the sample containing the stack with PMMA and *Electa 94* as before. We create the fine contacting structures by carefully aligning the sample in the lithography software using the previously created reference markers on the substrate. After developing the resist, 5 nm of chromium, followed by a 80 nm layer of gold is

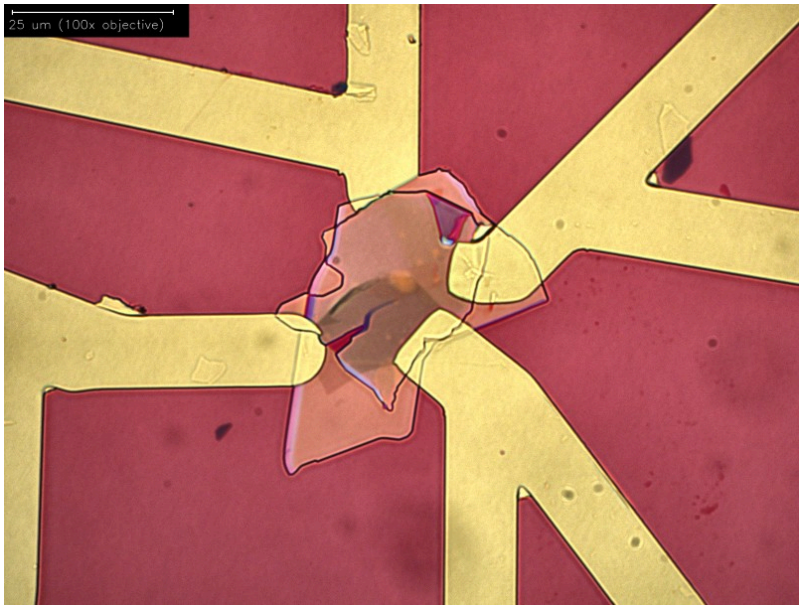

Figure 5.3: Microscope image of the 2D material stack after transfer onto the planar mirror substrate after the gold contacts have been deposited. The top hBN formed a large tear during the gold liftoff step.

deposited onto the sample via physical vapor deposition. After lift-off of the undeveloped areas, the desired gold structures remain on the sample, as shown in Figure 5.3.

In order to maximize the light-matter coupling strength g, the TMD monolayer must be positioned precisely at an antinode of the cavity's standing electromagnetic wave, where the field amplitude is maximal. We achieve this vertical positioning by placing the monolayer between two flakes of hexagonal boron nitride (hBN) of suitable thickness. Besides acting as a spacer, the hBN acts as an insulating layer to eventual electronic gates and provides structural support that prevents the monolayer from being damaged. When the 2D material stack is transferred onto the planar substrate, the bottom hBN flake determines the exact distance between the mirror surface and the TMD monolayer.

The optimal thickness for this bottom layer is determined by the optical properties of the underlying DBR. As introduced in Section 2.3, the optical field penetrates into the mirror stack prior to complete reflection, shifting the position of the first electric field antinode away from the physical boundary of the substrate. Consequently, the thickness of the bottom hBN flake must be chosen to match the distance to this first antinode, taking the wavelength-dependent reflection phase φ_{DBR} into account. In the case of our DBR coatings, the electric field has a node on the mirror surface at $\lambda = 760\,\mathrm{nm}$, which is the relevant wavelength for the exciton resonance in $MoSe_2$ [22]. For WSe_2, the phase shift at

the relevant wavelength $\lambda = 720\,\mathrm{nm}$ is $\varphi_{\mathrm{DBR}} = 0.23\pi$. If the bottom spacer deviates from this ideal thickness, the TMD will sit at a lower field amplitude, reducing the observable Rabi splitting. The top hBN layer also has to be matched to the target wavelength to preserve the cavity resonance condition. Because the surface of the hBN introduces an additional reflection within the resonator, its thickness must be matched to the operating wavelength to ensure that the reflection interferes constructively with the cavity field. This behavior is illustrated in Figure 5.4 and Figure 5.5. If a graphite flake is added on top of the stack to act as a top gate for exciton confinement experiments, the combined thickness of the hBN layers also has to position the graphite in a field node to minimize absorption losses.

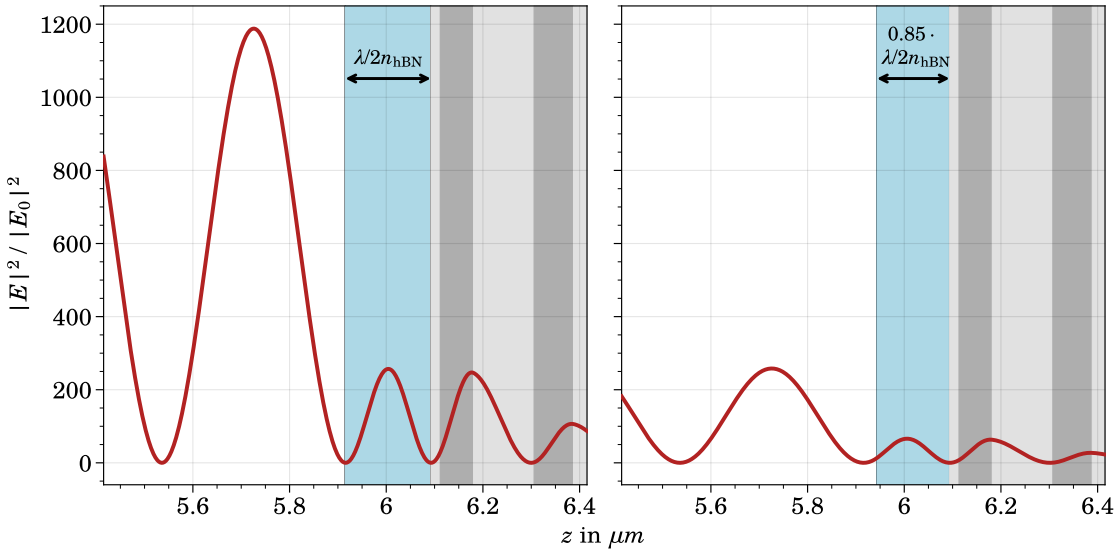

Figure 5.4: Transfer matrix simulation of the cavity intensity distribution at a wavelength of 760 nm with two layers of hBN (light blue) stacked on top of each other. The dark / light layers represent the high / low refractive index DBR layers. The length of the cavity is tuned to resonance in both cases. **Left:** The combined thickness of the hBN layers is matched to the wavelength. **Right:** The combined thickness of the hBN layers is mismatched by a factor of 0.85.

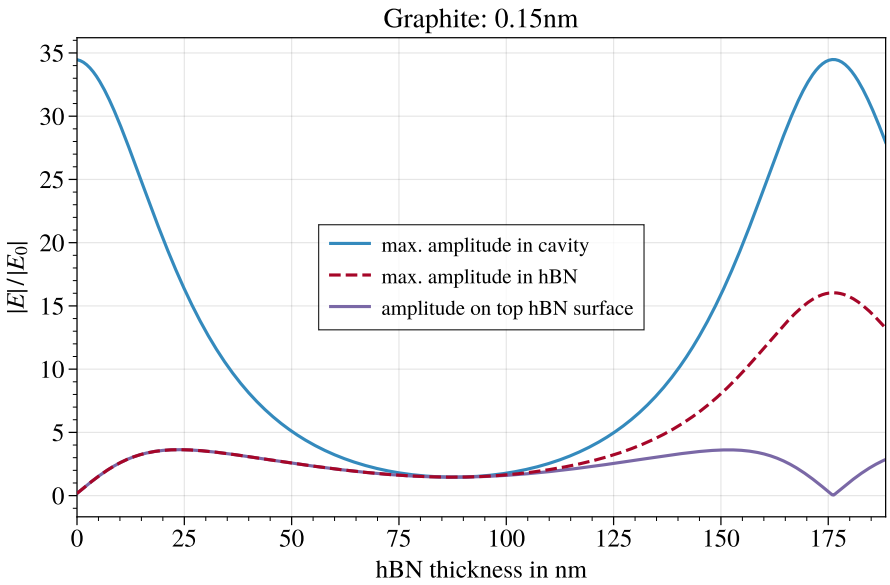

Figure 5.5: TMM simulation results of the cavity amplitude as a function of the hBN layer thickness.

5.2 Cryostat measurements

Following the room temperature assembly and characterization of the microcavity, the cavity scanner is inserted into the liquid-helium cryostat. Operating at cryogenic temperatures is essential for our experiments to suppress phonon scattering and minimize the linewidth of the excitonic resonances, which is necessary for the system to reach strong coupling. Once the assembly is inserted, the first challenge is to spatially locate the TMD monolayer sample on the planar substrate, since direct visual access is made difficult due to the high reflectivity of the planar mirror.

To identify the exact position of the TMD monolayer, we perform a raster scan of the optical transmission across the sample plane. In order to carry out the scan at a safe distance between fiber and substrate, while still getting enough transmission signal, the cavity length is tuned to a safe distance (in this case, approximately 13 µm) using the z-positioner. At each position, a transmission spectrum is recorded using broadband white light coupled into the cavity through the cavity fiber. By applying a window filter to the acquired spectra and then integrating the transmitted intensity over all wavelengths, a two-dimensional map of the spatial transmission profile is created, see Figure 5.6. The window filter reduces sharp features appearing in the map that can be caused by transmission peaks entering the recorded wavelength range due to slight height variations over the sample. The map shows clear features of the sample that are caused by the varying thickness and

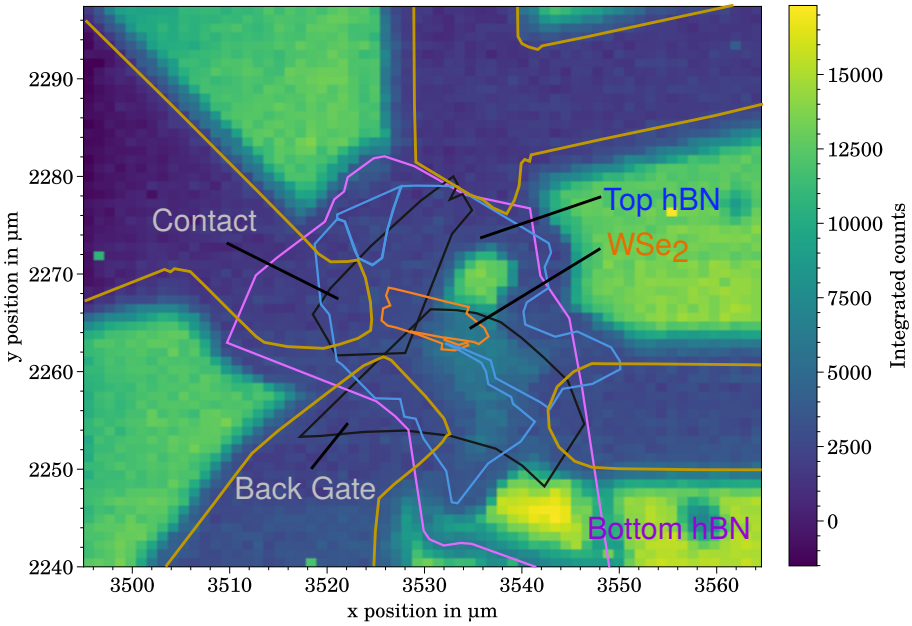

Figure 5.6: Raster scan of the sample in the cavity, measured by coupling in white light and recording a transmission spectrum at each location. For each pixel, the spectra are summed over all wavelengths after a window filter is applied (an example spectrum and window filter are shown in Figure A.3). The outlines of the flakes that make up the sample are overlaid, with the TMD monolayer at the center in orange. The resulting image is mirrored compared to the optical microscope image before due to the movement direction of the positioners.

refractive index of the 2D material stack and from the gold contacts. We can now determine the expected position of the monolayer by overlaying the map with the traced outlines of the flakes that make up the stack, which were documented in microscope images by the automatic flake-search.

Following the successful spatial mapping of the 2D material sample, we proceeded to search for signatures of strong light-matter interaction. By systematically tuning the cavity length across the relevant wavelength range, we successfully recorded transmission spectra and cavity resonances directly on the integrated WSe_2 sample. However, we were unable to observe the characteristic avoided crossing or vacuum Rabi splitting required to definitively confirm the formation of exciton-polaritons. We attribute this absence of the strong coupling regime primarily to the unfortunate structure of the integrated 2D material stack. As observed in the optical microscope images prior to the cryostat measurements, the individual flakes shifted during the transfer process, and a visible tear formed in the top hBN layer during the lithography process for applying the contacts. Furthermore, close inspection of the sample under a microscope suggest the presence of surface

contamination across the sample, likely caused by adhesive residue introduced during the mechanical exfoliation process. Because the bare fiber-based microcavity demonstrated the required high optical performance, future attempts should focus primarily on repeating the measurements with a sample that has a more ideal structure and is free of contamination.

CHAPTER 6

Conclusion and outlook

During this thesis, we successfully designed, fabricated, and characterized a highly tunable fiber-based microcavity system specifically designed for the investigation of exciton-polaritons in two-dimensional materials. Into this microcavity setup, we integrated a heterostructure containing a transition metal dichalcogenide (TMD) monolayer and cooled the setup down to cryogenic temperatures. After systematically optimizing the CO_2 laser ablation parameters and the chemical fiber preparation and mechanical cleaving, we established and carried out a fabrication routine for concave fiber mirrors with precisely engineered Gaussian dimple geometries: We produced a total of 144 fibers with radii of curvature (ROC) varying between 20 µm and 200 µm and depths between 0.06 µm and 2 µm. This range includes a variety of geometries that are suitable for constructing a cavity with which the strong coupling regime can be reached.

After the application of high-reflectivity distributed Bragg reflector (DBR) coatings, we integrated these mirrors into both an ambient testing setup and a custom-built cryogenic cavity setup. To build this cryogenic setup, we adapted a design from a group at ETH Zürich with some modifications and had the necessary parts made by the mechanical workshop of the Physical Institute. Both implementations provide the spatial degrees of freedom for accurately positioning the cavity mode on a planar sample, as well as tuning the cavity length for scanning the cavity resonance. Through extensive optical characterization, we verified the functionality of the cavity configuration including our fabricated fiber mirrors and demonstrated a maximum measured cavity finesse around 3000 in the final cryogenic scanner assembly.

With the cavity implementation complete, we proceeded to integrate a 2D material sample containing a WSe_2 monolayer encapsulated in hexagonal boron nitride (hBN). Using the fully assembled cavity scanner, we cooled the assembly down to cryogenic

temperatures and successfully measured cavity resonances directly on the sample and recorded a spatial map of the heterostructure through spectroscopic transmission measurements. We were not able to observe the characteristic avoided crossing, which would confirm the creation of exciton-polaritons. We attribute this absence of strong coupling to the suboptimal quality of the integrated sample: During the transfer process and subsequent lithography, the layers of the structure shifted and a visible crack formed in the top hBN layer, which possibly lead to a severe degradation of the exciton signal. Furthermore, optical microscopy indicated possible surface contamination across the sample, likely caused by adhesive residue introduced during the mechanical exfoliation process.

Future experimental efforts will focus on fabricating and integrating different TMD heterostructures with improved quality to reach the strong coupling regime. Another possible improvement would be further reduction of the cavity length and mode waist by engineering fiber dimples with an even shallower depth and smaller radius of curvature, which would require changes to the beam parameters of the CO_2 laser machining setup.

Looking ahead, the flexibility of our fiber-based cavity platform provides possibilities for further quantum optics research.

APPENDIX A

Figures

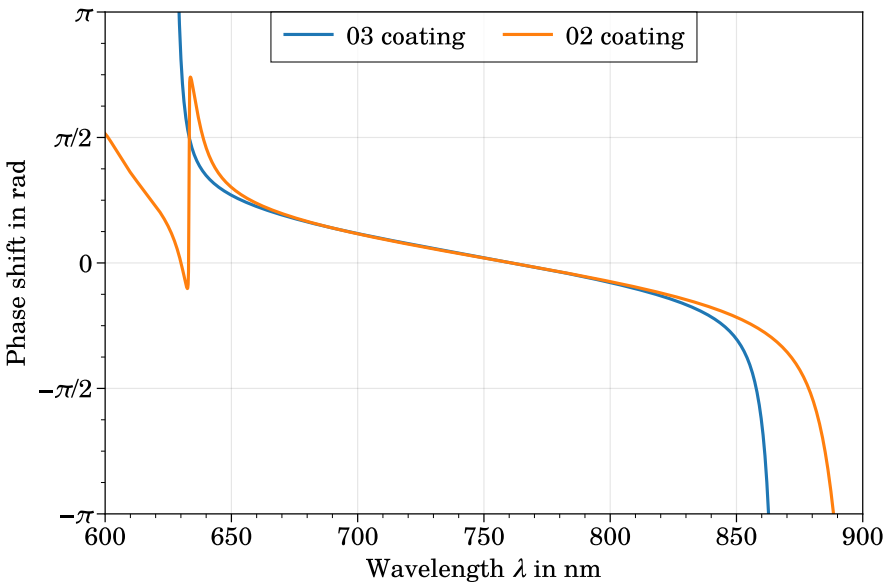

Figure A.1: Wavelength-dependent mirror phase shifts of our two DBR coatings, calculated using the transfer matrix method.

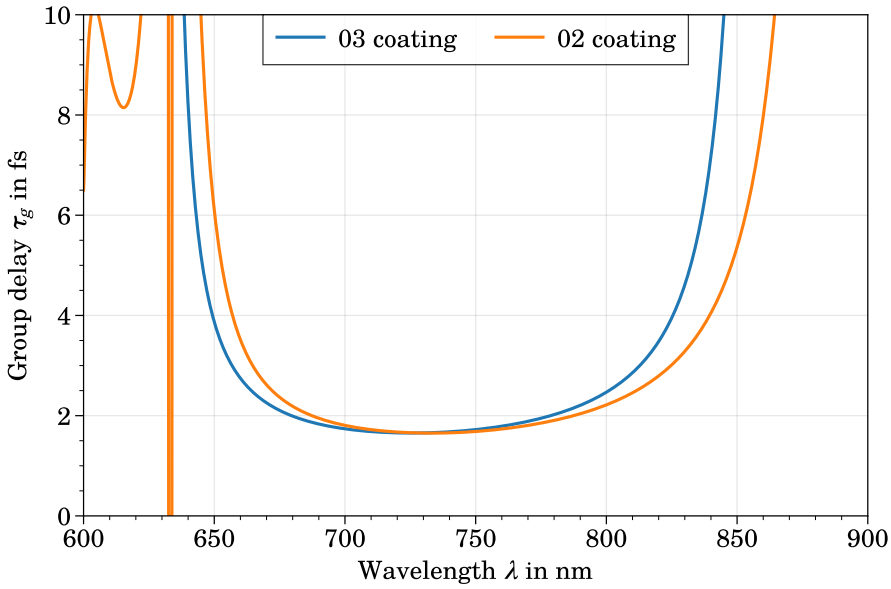

Figure A.2: Wavelength-dependent mirror group delays of our two DBR coatings, calculated using the transfer matrix method.

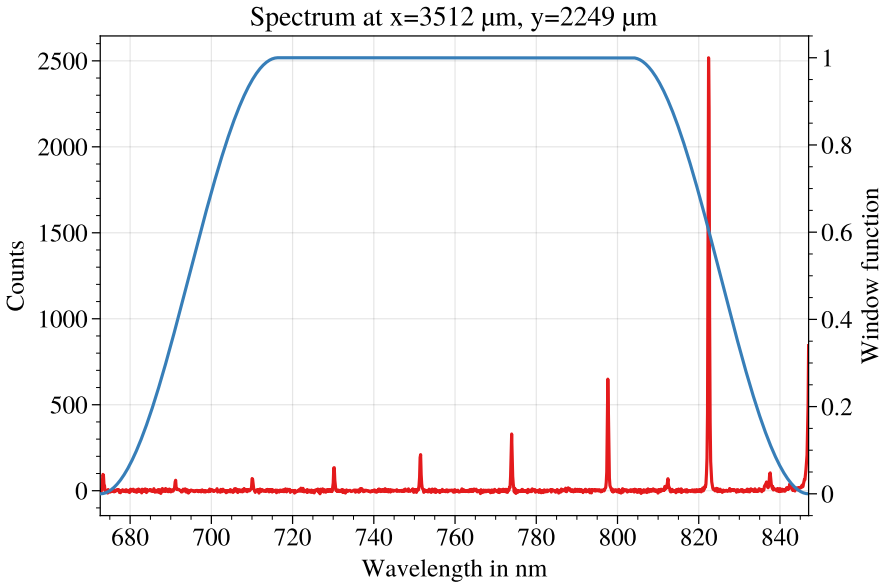

Figure A.3: Example of a spectrum recorded in the raster scan (Figure 5.6) with the window function that is multiplied with the data before integrating the counts.

Bibliography

[1] A. V. Kavokin, J. J. Baumberg, G. Malpuech, and F. P. Laussy, *Microcavities*, 2nd ed. (Oxford University Press, 2017).

[2] J. Kasprzak et al., Bose–Einstein condensation of exciton polaritons, Nature **443**, 409 (2006).

[3] G. Wang, A. Chernikov, M. M. Glazov, T. F. Heinz, X. Marie, T. Amand, and B. Urbaszek, Colloquium: Excitons in atomically thin transition metal dichalcogenides, Reviews of Modern Physics **90**, 21001 (2018).

[4] C. Schneider, M. M. Glazov, T. Korn, S. Höfling, and B. Urbaszek, Two-dimensional semiconductors in the regime of strong light-matter coupling, Nature Communications **9**, 2695 (2018).

[5] K. S. Novoselov, A. K. Geim, S. V. Morozov, D.-e. Jiang, Y. Zhang, S. V. Dubonos, I. V. Grigorieva, and A. A. Firsov, Electric field effect in atomically thin carbon films, Science **306**, 666 (2004).

[6] Q. H. Wang, K. Kalantar-Zadeh, A. Kis, J. N. Coleman, and M. S. Strano, Electronics and optoelectronics of two-dimensional transition metal dichalcogenides, Nature Nanotechnology **7**, 699 (2012).

[7] A. Chernikov, T. C. Berkelbach, H. M. Hill, A. Rigosi, Y. Li, O. Aslan, D. R. Reichman, and T. F. Heinz, Exciton Binding Energy and Nonhydrogenic Rydberg Series in Monolayer WS2, Phys. Rev. Lett. **113**, 76802 (2014).

[8] X. Liu, T. Galfsky, Z. Sun, F. Xia, E.-c. Lin, Y.-H. Lee, S. Kéna-Cohen, and V. M. Menon, Strong light–matter coupling in two-dimensional atomic crystals, Nature Photonics **9**, 30 (2015).

[9] S. Dufferwiel et al., Exciton-polaritons in van der Waals heterostructures embedded in tunable microcavities, Nature Communications **6**, 8579 (2015).

[10] D. Hunger, T. Steinmetz, Y. Colombe, C. Deutsch, T. W. Hänsch, and J. Reichel, A fiber Fabry-Perot cavity with high finesse, New Journal of Physics **12**, 65038 (2010).

[11] M. Selig, G. Berghäuser, A. Raja, P. Nagler, C. Schüller, T. Korn, A. Chernikov, E. Malic, and A. Knorr, Excitonic linewidth and coherence lifetime in monolayer transition metal dichalcogenides, Nature Communications **7**, 13279 (2016).

[12] L. B. Tan, Interacting Fermi and Bose Exciton-Polaron-Polaritons, Doctoral dissertation, 2022.

[13] I. Carusotto and C. Ciuti, Quantum fluids of light, Reviews of Modern Physics **85**, 299 (2013).

[14] H. Deng, H. Haug, and Y. Yamamoto, Exciton-polariton bose-einstein condensation, Reviews of Modern Physics **82**, 1489 (2010).

[15] B. E. A. Saleh and M. C. Teich, *Fundamentals of Photonics: Part 1: Optics; 3rd Edition* (Wiley, Hoboken, 2019).

[16] C. Koks and M. P. van Exter, Microcavity resonance condition, quality factor, and mode volume are determined by different penetration depths, Optics Express **29**, 6879 (2021).

[17] M. Scharfstädt, Implementation of a Micro-Mirror Production Setup for Quantum Information Applications, Master's thesis, 2022.

[18] A. Bick, C. Staarmann, P. Christoph, O. Hellmig, J. Heinze, K. Sengstock, and C. Becker, The role of mode match in fiber cavities, Review of Scientific Instruments **87**, (2016).

[19] O. A. Ajayi, J. V. Ardelean, G. D. Shepard, J. Wang, A. Antony, T. Taniguchi, K. Watanabe, T. F. Heinz, and J. C. Hone, Approaching the intrinsic photoluminescence linewidth in transition metal dichalcogenide monolayers, 2d Materials **4**, 31011 (2017).

[20] G. Scuri et al., Large excitonic reflectivity of monolayer MoSe2 encapsulated in hexagonal boron nitride, Physical Review Letters **120**, 37402 (2018).

[21] Z. Li et al., Revealing the biexciton and trion-exciton complexes in BN encapsulated WSe2, Nature Communications **9**, 3719 (2018).

[22] M. Wegerhoff, M. Scharfstädt, S. Linden, and A. Bergschneider, Coherent Interaction of 2 s and 1 s Exciton States in Transition-Metal Dichalcogenide Monolayers, Physical Review Letters **134**, 236901 (2025).